https://doi.org/10.5194/egusphere-2025-4818
Preprint. Discussion started: 5 November 2025

Measurement report: Altitudinal Shift of Ozone Regimes in a Mountainous Background Region

Yuan Yang[1], Haibo Li[2,3], Yonghong Wang[4*], Hao Zhang[5], Zhou Yang[6], Xiangwen Hou[2,3], Dan Yao[7], Hong Hu[1], Keyong Zhu[1], Ya Xiong[1], Li Lai[1], Dengmei Chen[1], Peisong Feng[1]

[1]Guizhou Research and Designing Institute of Environmental Sciences, Guizhou Academy of Environmental Science and Design, Guiyang, China

[2]Fanjingshan National Nature Reserve Administration, Tongren, Guizhou, China

[3]Guizhou Fanjingshan Forest Ecosystem Observation and Research Station, Tongren, Guizhou, China

[4]Laboratory of Atmospheric Environment and Pollution Control, Research Center for Eco-Environmental Sciences, Chinese Academy of Sciences, Beijing, China

[5]School of Public Health, Shandong Second Medical University, Weifang, Shandong, China

[6]Tongren University, Tongren, Guizhou, China

[7]Key Laboratory of Yellow River and Huai River Water Environment and Pollution Control, Ministry of Education, Henan Key Laboratory for Environmental Pollution Control, School of Environment, Henan Normal University, Xinxiang, Henan, China

Correspondence: yonghongwang@rcees.ac.cn

Abstract: Elevated background ozone (O_3) poses significant challenges for regional air quality management. Understanding the vertical distribution of O_3 and its precursors is critical yet underexplored in Southwest China. This study presents the first comprehensive altitudinal gradient analysis (550 m, 1,774 m, 2,119 m a.s.l.) in the Fanjingshan National Nature Reserve, a remote high-altitude site on the Yunnan-Guizhou Plateau. Continuous measurements (March-August 2024) revealed a marked positive gradient in O_3 (14.8 ± 15.2 ppb at mountain foot to 40.2 ± 14.7 ppb at mountaintop), contrasting with declining precursor concentrations. Random Forest–SHAP analysis identified relative humidity and NO_x as dominant controls at the mountain foot, whereas temperature and reactive VOCs governed O_3 variability aloft. Chemical box modeling (OBM-MCM v3.3.1) demonstrated net O_3 destruction at mountain foot (−1.93 ppb hr^{-1}) due to NO titration, shifting to net production at mountainside (0.35 ppb hr^{-1}) and mountaintop (0.29 ppb hr^{-1}). While O_3 formation remained NO_x-limited across all sites, sensitivity to anthropogenic hydrocarbons increased with altitude (RIR: -0.12 mountain foot to 0.51 mountaintop). Transport analysis indicated O_3 accumulation at mountain foot via regional transport, contrasting with mountainside and mountaintop, which function as net source regions. These findings necessitate altitude-specific O_3 control: prioritizing NO_x reduction at lower elevations while coordinating NO_x and VOC controls at higher altitudes. Expanding high-altitude monitoring, especially in under-monitored areas like Southwest China, is crucial for characterizing regional background pollution. Future studies require vertical monitoring with improved models to assess transboundary impacts and changing emissions.

Key words: Vertical Ozone Profiling; Ozone precursors; Photochemical Mechanisms; Regional Transport; Mount Fanjing

1 Introduction

Ozone (O_3) within the atmospheric boundary layer results from the disruption of fundamental NO-NO_2-O_3 photochemical cycles through radical generation and transport processes under combined thermodynamic and dynamic factors (Atkinson and Arey, 2003; Carter, 2012). It exerts significant influences on biogeochemical cycles, vegetation net primary productivity, climate forcing, air quality, and human health (Feng et al., 2022; Tong et al., 2023; Feng et al., 2015; Wang et al., 2020; Wang et al., 2014). Although previous studies have demonstrated that regulating precursor emissions following the EKMA curve can mitigate photochemical pollution, control measures may fail due to neglecting the influence of horizontal regional transport, vertical exchange on O_3 and its precursor concentrations. However, conventional ambient air quality monitoring stations for O_3 are typically ground-based, and their fluctuating measurements cannot fully capture the spatial distribution of O_3 in both horizontal and vertical dimensions, thereby limiting their utility for air quality forecasting and the formulation of pollution control strategies. In key regions and megacities, rare vertical profiles of O_3 and its precursors have been obtained using platforms such as tethered balloons, manned/unmanned aircraft, and meteorological gradient towers (Dieu Hien et al., 2019; Li et al., 2022; Mo et al., 2022; Xue et al., 2011a). Undoubtedly, vertical profiles from tethered balloons, aircraft campaigns, and meteorological towers have significantly advanced our understanding of anthropogenic influences on large-

https://doi.org/10.5194/egusphere-2025-4818
Preprint. Discussion started: 5 November 2025

scale atmospheric processes and enriched theories of tropospheric chemistry and transport (Wang et al., 2025; Andreae et al., 2015; He et al., 2023; Shtabkin et al., 2020; Shi et al., 2019). However, none of these platforms can fully resolve the three-dimensional distribution of O_3 pollution or reliably reflect regional pollution levels and dynamics.

High-altitude mountain atmospheres are less influenced by surrounding ground-level pollution sources, making them suitable for studying pollutant transport and the exchange between the atmospheric boundary layer and the free troposphere. Observations from these sites better reflect regional pollution levels and their variations (Kanaya et al., 2013), while also serving as ideal locations for diagnosing and quantifying the impact of stratosphere-troposphere exchange on lower tropospheric O_3. To date, intensive observational studies have been carried out at several high-altitude mountain stations, such as Mt. Kenya, Mt. Waliguan, Mt. Abu, Mt. Happo, Mt. Bachelor Observatory, Sonnblick, Tanah Rata, Kislovodsk, Krvavec, Arosa, and Pico Mountain Observatory(Okamoto and Tanimoto, 2016). These studies focus on background concentrations of O_3 and its precursors, as well as temporal variations in long-range transport, and meteorological mechanisms. Regarding O_3 background concentrations, measurements from dozens of global observation stations indicate that near-surface O_3 levels in the Northern Hemisphere range between 20-60 ppbv, with specific concentrations varying by geographic location, altitude, and anthropogenic influence (Gaudel et al., 2020). Temporally, regional background and high-altitude stations exhibit increasing trends in mean O_3 concentrations, peak values, exceedance frequencies, and durations of high-O_3 episodes (Cooper et al., 2020). In summary, high-altitude observational campaigns employing multi-platform measurements, coupled with comprehensive analysis and modeling, have advanced our systematic understanding of upper lower-tropospheric air pollution and atmospheric chemistry. These efforts have enhanced knowledge of O_3 and precursors background concentrations, trends, and long-range transport dynamics. However, existing high-altitude stations are unevenly distributed globally, with most located in mid-latitudes. Expanding the global observational network through additional high-altitude stations will be crucial to improving O_3 and precursors monitoring and modeling capabilities. Since the 1990s, China has successively established regional atmospheric background monitoring stations at Longfengshan, Lin'an, Mt. Waliguan, Mt. Tai, Mt. Huang, Mt. Hua, and Mt. Heng, obtaining systematic observational datasets with regional characteristics (Kanaya et al., 2013; Xue et al., 2013; Xue et al., 2011b; Yang et al., 2017; Li et al., 2020). During the summer of 2006, Japanese and domestic researchers collaborated on a comprehensive atmospheric chemistry campaign (MTX2006) at Mt. Tai, providing in-depth insights into photochemical pollution, aerosol physicochemical properties, and the contributions of biomass burning and biogenic emissions to regional pollution (Kanaya et al., 2013). Additionally, Chinese and Japanese researchers conducted continuous measurements of O_3 and CO at Mt. Huang and Mt. Hua, employing observational and modeling approaches to study photochemical pollution in eastern China (Wang et al., 2006). Despite recent advances, critical observational gaps persist, including a sparse high-altitude monitoring network-particularly sparse over southwestern China compared to global standards, a predominance of near-surface measurements of ozone and its precursors with scarce data in the crucial 1000–2000 m layer, and a general lack of vertically resolved analyses of these species. Therefore, it is helpful to establish gradient observation stations at high altitudes of more than 2000 m on the plateau to carry out gradient observation research on O_3 and its precursors, which can help to accurately formulate regional background photochemical pollution control strategies.

Mt. Fanjing is the highest peak in the transitional slope between the Yunnan-Guizhou Plateau and the western Hunan hills, located in northeastern Guizhou Province, China. The summit reaches an elevation of 2570 m a.s.l., while the lowest point is at 500 m a.s.l., resulting in a topographic relief of over 2000 m. This area is influenced by both the Pacific Southeast Monsoon and the Indian Ocean Southwest Monsoon, creating a climatic convergence zone. The fluctuating temperature-humidity regimes provide critical conditions for the overlapping distribution of flora from different biogeographic regions. To investigate the influence of latitudinal zonality, vertical zonality, and slope aspect on meteorological conditions, as well as to comprehensively monitor meteorological dynamics under varying geographic conditions, the Mt. Fanjing Administration established and upgraded a multi-parameter observation network between 2012 and 2013. Due to its remoteness from anthropogenic pollution sources, Mt. Fanjing excellent environmental quality and serves as a relatively "clean area". The protection and study of this pristine environment will provide valuable insights into atmospheric chemistry in background regions and support air pollution control strategies. However, to date, no project has investigated the vertical gradient

https://doi.org/10.5194/egusphere-2025-4818
Preprint. Discussion started: 5 November 2025

characteristics of O_3 and its precursors. In this study, leveraging the three-dimensional meteorological monitoring system of Mt. Fanjing, we established a gradient observation platform for atmospheric pollutants at the mountain foot, mountainside, and mountaintop, enabling the observation and analysis of vertical profiles of O_3 and its precursors. The main aim of this study is to better understanding the altitudinal gradient variations of O_3 production rates and sensitives. The findings will provide scientific support for the management of regional photochemical pollution and the conservation of ecological integrity in protected areas at the national level.

2 Materials and methods

2.1 Sampling location description

In March 2024, leveraging automated weather stations in the core zone of the Fanjingshan National Nature Reserve, we established observation sites for O_3 and its precursors at Heiwanhe (mountain-foot observatory: 27°50′45″N, 108°46′3.87″E; 550 m a.s.l.), Huixiangping (mountainside observatory: 27°54′6.46″N, 108°42′14.33″E; 1,774 m a.s.l.), and the upper cable car station (mountaintop observatory: 27°54′36.59″N, 108°41′44.50″E; 2,119 m a.s.l.) ***(Figure 1)***. The mountain-foot observatory is adjacent to the eastern gate of the Fanjingshan Scenic Area, with surrounding homestays and dining facilities to the south. Approximately 150 m east of the station lies an eco-friendly sightseeing vehicle route, while the Heiwan River. The mountainside observations were conducted at the Huixiangping Forest Meteorological Station. This site serves as a resting platform for hikers and is situated in a north-subtropical climate. The mountaintop observatory is positioned at the Wanbaoyan viewing platform near the upper cable car station. Within a 200 m radius, minor service facilities, including small restaurants and shops, exist. Collectively, the vertical gradient monitoring stations for O_3 and its precursors on Mt. Fanjing are situated far from anthropogenic sources. The observational data thus reliably represent the general altitudinal distribution patterns of O_3 and its precursors in the background region of the Yunnan-Guizhou Plateau. From March 1st to August 31th 2024, continuous measurements were conducted for O_3, NO_x, CO, 57 VOCs species, and meteorological parameters.

2.2 In-situ synchronous observations of O_3 and its precursors

O_3 concentrations were quantified employing a ultraviolet (UV) absorption spectrometer (EAQM-3000; Jiangsu Skyray Instrument Co., Ltd., Jiangsu, China), a gold-standard technique recognized for its exceptional precision in tropospheric ozone monitoring. NO and NO_2 were detected using a high-resolution chemiluminescence analyzer (EAQM-2000; Jiangsu Skyray Instrument Co., Ltd., Jiangsu, China), specifically optimized for precise measurement of trace atmospheric constituents. CO levels were determined via a non-dispersive infrared photometer (EAQM-4000; Jiangsu Skyray Instrument Co., Ltd., Jiangsu, China) incorporating gas filter correlation technology, significantly improving molecular specificity and minimizing cross-interference from other atmospheric gases. All analytical instruments were subjected to rigorous calibration procedures. The experimental design and analytical methodology strictly adhered to China's National Environmental Protection Standards, with all QA/QC protocols implemented in accordance with Class I monitoring station requirements as stipulated by the Ministry of Ecology and Environment of China. Meteorological parameters, including ambient temperature, relative humidity, atmospheric pressure, wind speed and wind direction, were continuously monitored and recorded using an automated weather station (WZZ-M6; Jiangsu Weizhihuan Energy Technology Co., Ltd., Jiangsu, China).

VOCs were measured in real time using an Ntrace VsCMS6500 VOCs automated monitoring system (Ntrace VsCMS6500; Nutech (China) Co.,Ltd., Changsha, China). The instrument employs a unique “dual-column separation + center cutting + single FID” design, enabling comprehensive separation and analysis of VOCs compounds. Ambient air or calibration gas is introduced at a constant flow rate into the sampling system, where interfering substances are removed via cryogenic trapping, followed by enrichment of target analytes. Subsequently, the enriched compounds are thermally desorbed, separated by gas chromatography (GC), and quantified using a hydrogen flame ionization detector (FID). External standard calibration was applied for quantification. A series of standard gases (0.5, 2, 4, 6, 8, and 10 nmol/mol) were analyzed in triplicate from low to high concentrations. Calibration curves were constructed using least-squares regression, with target compound concentrations as the abscissa and peak areas as the ordinate. The correlation coefficients (R^2) of all calibration curves were ≥0.98. The relative error between the measured and reference values at the lowest calibration point was ≤15%. Method

https://doi.org/10.5194/egusphere-2025-4818
Preprint. Discussion started: 5 November 2025

detection limit (MDL): ≤0.1 nmol/mol for 90% of the species. In summary, the system enables continuous sampling, processing, and detection of ambient VOCs, providing reliable quantification of 57 photochemical precursors.

2.3 Random forest modeling and SHAP-based interpretation

Random Forest (RF), an ensemble learning algorithm, improves predictive accuracy and robustness by aggregating predictions from multiple decision trees (Breiman, 2001; Zhang et al., 2025). The method employs bootstrap sampling and random feature selection to generate diverse trees, reducing overfitting while remaining applicable to both classification and regression tasks. Feature importance is quantified via two primary metrics: (1) the mean decrease in impurity (e.g., Gini index or entropy) at nodes where a feature splits data, or (2) the reduction in out-of-bag accuracy upon feature permutation. We implemented RF to evaluate meteorological and precursor drivers of O_3 variability using the R packages "randomForest", "rfPermute", and "A3". A fixed random seed (123) ensured reproducibility. Initial parameter optimization used a 7:3 training-validation split, with the final model trained on the full dataset (parameters: importance = TRUE, ntree = 500, nrep = 1000). Model significance and cross-validated R^2 were assessed via 1,000 permutation tests. To elucidate the sensitivity and response dynamics between predictor variables and outcomes within the RF model, we applied SHAP (Shapley Additive Explanations), which provide both local and global insights, elucidating nonlinear predictor-response relationships in complex models like RF (Lundberg et al., 2020). In our analysis, positive SHAP values indicate O_3-enhancing effects, while negative values denote suppression, with magnitudes reflecting relative contribution strength.

2.4 Concentration-Weighted Trajectory CWT model

The Concentration-Weighted Trajectory (CWT) model has been widely employed to evaluate the regional transport of air pollutants by integrating backward trajectory analysis with observed chemical concentration data(Xing et al., 2024; Wu et al., 2025; Zhu et al., 2023; Jain et al., 2023; Seibert et al., 1994). Prior to conducting CWT analyses, backward trajectories were computed for each sampling site. The requisite meteorological input datasets for the HYSPLIT model (v4.9 Hybrid Single-Particle Lagrangian Integrated Trajectory) were obtained from the National Oceanic and Atmospheric Administration (NOAA) Global Data Assimilation System (GDAS) archive (available at ftp://arlftp.arlhq.noaa.gov/pub/archives/gdas1; last accessed: 25 May 2025). For the backward trajectory analysis, 36-h air masses arriving at each monitoring site during the sampling period were simulated, with 24 hourly initiations per day (from 00:00 to 23:00 UTC) at a temporal resolution of 1 hour. For CWT analysis, we employed the widely-used "openair" R package, which provides a user-friendly interface for comprehensive air quality data analysis. Additional technical specifications pertaining to the CWT methodology are available in previously published works (Zheng et al., 2019; Zheng et al., 2018).

2.5 Observation-based chemical box model

Comprehensive analysis of in situ O_3 production and loss pathways, and O_3 formation regime was conducted through an Observation-Based Model (OBM) framework integrated with the Master Chemical Mechanism (MCM v3.3.1), hereafter referred to as OBM-MCM. The detailed chemical mechanism, publicly available through the MCM repository (http://mcm.york.ac.uk, accessed 19 May 2025), encompasses an extensive reaction network comprising >5,800 chemical species participating in approximately 17,000 elementary reactions. Photolysis rate coefficients (J-values) were parameterized as a function of solar zenith angle and altitude using high-resolution lookup tables precomputed by the Tropospheric Ultraviolet and Visible radiative transfer model (Wolfe et al., 2016). Although the model explicitly accounted for boundary layer dilution processes, the zero-dimensional (0-D) formulation inherently excluded both vertical and horizontal advective transport mechanisms. Model constraints were rigorously defined by empirically measured meteorological parameters (temperature, relative humidity, and pressure) and precisely quantified trace gas concentrations (NO, NO_2, CO, and speciated VOCs). To minimize initialization artifacts and achieve robust chemical steady-state conditions, all simulations incorporated a 72-hour spin-up period prior to formal analysis.

High-temporal-resolution observational data encompassing O_3, NO_x, CO, speciated VOCs, along with meteorological parameters (temperature, relative humidity, pressure) and photochemically derived J_{NO_2} values were employed as inputs for

https://doi.org/10.5194/egusphere-2025-4818
Preprint. Discussion started: 5 November 2025

the OBM-MCM. This framework enabled precise quantification of in situ O_3 formation and consumption kinetics. To address the confounding influence of NO-mediated O_3 titration, we computed the net formation rate of odd oxygen ($O_3 + NO_2$) rather than considering O_3 in isolation. Each simulation incorporated a four-day model spin-up period to achieve thermodynamic equilibrium for unmeasured reactive intermediates, particularly hydroxyl radicals (OH), thereby ensuring robust chemical initialization. The relative contributions of local photochemical production versus regional transport were analytically decoupled through the relation: $R_{trans} = R_{meas} - R_{chem}$, where R_{trans} represents transport-derived flux, R_{meas} denotes observed O_3 variation, and R_{chem} signifies chemically driven formation rates. Comprehensive details regarding the computational chemistry methodology are available in the literature (Zhou et al., 2024; Zhong et al., 2025; Liu et al., 2022; Chen et al., 2020; Xue et al., 2014). Mechanistic analysis revealed that O_3 production primarily occurred via NO_x oxidation by peroxy radicals (HO_2 + RO_2), while dominant loss pathways involved photolytic decomposition coupled with reactive depletion through NO_2, OH, HO_2 and unsaturated VOCs.

The relationship between O_3 and its precursors was rigorously evaluated using two complementary approaches: 1) The relative incremental reactivity (RIR), a diagnostic metric for assessing the sensitivity of O_3 formation to precursor emissions, is defined as the ratio of the change in O_3 production rate to the corresponding change in precursor concentration (Liu et al., 2020; Lu et al., 2019; Guo et al., 2017; Wang et al., 2017). 2) The Empirical Kinetics Modeling Approach (EKMA), which facilitated systematic mapping of O_3-NO_x-VOC response surfaces to identify optimal emission control strategies. For each pollution episode, baseline conditions were established through temporal averaging of diurnal measurement profiles, forming the foundation for subsequent perturbation modeling. Our comprehensive sensitivity analysis employed a factorial design with 400 discrete emission scenarios, methodically varying anthropogenic hydrocarbon (AHC) and NO_x concentrations from ambient levels to 200% in 10% increments. This ensemble approach enabled high-resolution mapping of maximum O_3 formation isopleths, revealing the nonlinear coupling between precursor emissions and O_3 production.

3 Results and discussions

3.1 Observational overview

Mt. Fanjing exhibits a steep vertical meteorological gradient, manifesting as distinct conditions across altitudes: typically sunny conditions mountain foot, fog enveloping mountainside, and frequent rainfall at mountaintop ***(Figures S1–S3)***. Observational data revealed inverse altitudinal gradients for both wind speed and atmospheric pressure relative to temperature. Measured temperatures were 22.4±5.1, 16.8±4.2, and 15.0±3.9°C at mountain foot, mountainside, and mountaintop, respectively ***(Figure 2A)***. Corresponding atmospheric pressures were 945±4.5, 819±2.8, and 783±2.6 hPa ***(Figure 2D)***, while corresponding wind speeds were 0.6±0.4, 0.7±0.6, and 1.4±1.4 m s^{-1} ***(Figure 2B)***. Relative humidity peaked at mountainside (91.7±9.7%), followed by the mountaintop (90.1±9.7%), and was lowest at mountain foot (86.5±12.2%) ***(Figure 2C)***. These observed vertical gradients in meteorological parameters may govern O_3 dynamics through modulation of both in-situ photochemical processes and advective transport mechanisms.

The campaign-averaged O_3 concentrations at mountain foot, mountainside, and mountaintop were 14.8±15.2, 30.4±13.4, and 40.2±14.7 ppb, respectively, demonstrating a pronounced positive altitudinal gradient ***(Figure 2E)***. The measurements revealed significantly lower O_3 concentrations at mountain foot and mountainside relative to corresponding elevations on Mt. Tai (Xue et al., 2022; Wu et al., 2024) and Mt. Hua (Wu et al., 2025), underscoring the differential influence of regional pollution background and local photochemical processes on mountain atmospheric composition. The O_3 concentration measured at mountaintop was closely comparable to the national average background O_3 concentration (40.3 ± 11.9 ppb)(Chen et al., 2025). This alignment indicates that the high-altitude atmospheric environment at this site functions as an effective regional receptor for well-mixed tropospheric air masses, minimally influenced by proximal emission sources. As shown in ***Figure 3***, the O_3 concentrations at mountaintop significantly exceeded those at Tanah Rata , La Quiaca Observatorio , Mt. Kenya and Lulin (Okamoto and Tanimoto, 2016), approached levels observed at Assekrem , Mt. Abu and Mt. Huang(Okamoto and Tanimoto, 2016; Gao et al., 2017; Li et al., 2007), but remained substantially lower than those recorded at Mt. Bachelor Observatory, Mt. Hua, Mt. Waliguan, Mt. Happo, Jungfraujoch, Monte Cimone, Nanling, Mt. Tai, and Shennongjia(Gong et

https://doi.org/10.5194/egusphere-2025-4818
Preprint. Discussion started: 5 November 2025

al., 2018; Lyu et al., 2021; Okamoto and Tanimoto, 2016; Sun et al., 2016; Xu et al., 2016). In contrast to O_3, concentrations of precursors demonstrated a pronounced negative altitudinal gradient, declining progressively from the mountain foot to the mountainside, and mountaintop. Measured concentrations were as follows: VOCs (12.8±8.3, 5.1±1.9, 9.4±25.4 ppb) ***(Figure 2F)***, NO_x (8.0±11.8, 1.2±3.8, 1.3±1.7 ppb) ***(Figure 2G)***, and CO (0.4±0.2, 0.3±0.5, 0.3±0.2 ppm) ***(Figure 2H)*** at mountain foot, mountainside, and mountaintop, respectively. The CO concentrations at mountaintop were significantly higher than those recorded at Mt. Happo, Izaña, Zugspitze-Gipfel (Okamoto and Tanimoto, 2016), but marginally lower than levels observed at Mt. Tai (Wu et al., 2024; Kanaya et al., 2013). This pattern underscores the interplay between localized human activities, geographic context, and chemical processes in mountain environments. The atmospheric reactivity of VOCs reflects each species's ability to participate in chemical reactions. The total calculated OH reactivity were 4.4, 1.5, and 2.0 s^{-1} at mountain foot, mountainside, and mountaintop, respectively ***(Figure S4A)***. The OH reactivity in this study was significantly lower than values observed at comparable altitudes of Mt. Tai (Wu et al., 2024) and in major Chinese cities including Beijing, Shanghai, Guangzhou, Chongqing, and Xianghe (Yang et al., 2020; Tan et al., 2019). While alkanes constituted the major fraction of VOCs concentrations-accounting for 43%, 57%, and 51% at mountain foot, mountainside, and mountaintop, respectively ***(Figure S5A-C)***-they drove only 8%, 13%, and 16% of the total OH reactivity at these elevations ***(Figure S4B and Figure S5D-F)***. In contrast, isoprene contributed minimally to VOCs concentrations (3%, 3%, and 1% at mountain foot, mountainside, and mountaintop), yet dominated OH reactivity, accounting for 26%, 46%, and 31% respectively ***(Figure S4D and Figure S5D-F)***, revealing a striking decoupling between concentration abundance and chemical reactivity. Alkenes and aromatics contributed 41% and 25%, respectively, to the OH reactivity at the mountain foot; 13% and 28% at mountainside; and 28% and 25% at mountaintop ***(Figure S4B, E and Figure S5D-F)***. Altitudinal variations in reactive VOCs species may drive corresponding differences in photochemical O_3 production.

Meteorological parameters at both mountainside and mountaintop exhibited similar diurnal variations without statistically significant magnitudes. Slight increases in temperature were observed during the daytime, accompanied by slight decreases in wind speed and relative humidity. The diurnal temperature ranges (difference between daytime and nighttime) were 6.8% and 10.8% for the mountainside and mountaintop, respectively ***(Figure 4A)***. Corresponding diurnal changes in wind speed were -2.0% and -0.4% ***(Figure 4B)***, and for relative humidity, -1.3% and -3.2% ***(Figure 4C)***. Contrastively, significant diurnal variations were observed in temperature, wind speed and relative humidity at mountain foot, with amplitudes of 16%, 47% and -11%, respectively ***(Figure 4A-C)***.

O_3 concentrations revealed pronounced diurnal heterogeneity across altitudinal gradients, characterized by elevated daytime levels at mountain foot contrasting with nocturnal maxima at mountainside and mountaintop ***(Figure 4D)***. At mountain foot, O_3 concentrations exhibited a unimodal diurnal cycle with concentrations rising steadily from 08:00 local time, peaking at 13:00, maintaining stability until 15:00, then declining to morning baseline levels. In contrast, mountainside and mountaintop O_3 concentrations remained relatively stable with synchronous diurnal cycles: gradual depletion commencing at 08:00, reaching minima near 15:00, followed by progressive recovery to morning concentrations. Notably, during the 12:00-16:00 interval, mountainside minima approached peak concentrations observed at mountain foot, while mountaintop levels significantly exceeded those at both lower elevations. This elevational divergence underscores complex interplay among boundary layer evolution, precursor advection, altitudinal transport pathways, mountain-valley circulations, and synoptic influences in modulating O_3 behavior. O_3 precursor species exhibited a pronounced bimodal diurnal pattern at mountain foot ***(Figure 4E-G)***. A primary concentration peak occurs during 08:00-09:00, followed by a secondary peak at 19:00–20:00, closely synchronized with tourist influx. Notably, the morning peak in VOCs concentrations at mountaintop lags the mountain foot peak by approximately 1-2 hours. This temporal offset suggests a delay in pollutant accumulation at higher altitudes due to boundary layer transport processes. In contrast, the mountainside, experiencing minimal anthropogenic disturbance (limited to occasional hikers), displayed significantly attenuated diurnal concentration variations in O_3 precursors. The observed non-uniform diurnal variations in O_3 and its precursors across elevational gradients reflect emergent phenomena driven by elevation-dependent shifts in precursor sources, spatially heterogeneous photochemical modulation by solar radiation and temperature, and complex mountain boundary-layer dynamics-including vertical transport, mixing, and altitude-varying sink

https://doi.org/10.5194/egusphere-2025-4818
Preprint. Discussion started: 5 November 2025

strengths through deposition.

3.2 Feature Importance Affecting O_3

The feature importance ranking for O_3 as the dependent variable is presented in ***Figure 5A-C***. The top five features were: relative humidity, NO_x, wind speed, temperature, and pressure at mountain foot ***(Figure 5A)***; temperature, relative humidity, VOCs, CO, and NO_x at mountainside ***(Figure 5B)***; and temperature, relative humidity, wind speed, VOCs, and wind direction at mountaintop ***(Figure 5C)***. Overall, meteorological factors exerted a consistently greater overall influence than chemical factors, underscoring the significance of meteorological factors in O_3 variability across the elevation gradient. ***Figure 5D-F*** displays SHAP summary plots for key features within the random forest model, corresponding to the mountain foot, mountainside, and mountaintop, respectively. These plots characterize the relative influence magnitude, feature prevalence, and effect direction of each variable on predicted O_3 concentrations. SHAP values farther from zero denote stronger feature importance; positive values indicate a positive association with O_3 levels, whereas negative values reflect an inverse relationship. For instance, elevated relative humidity corresponds to diminished SHAP values, indicating an inverse correlation between relative humidity and O_3 concentration. This likely arises from the complex interplay of physical and chemical processes, such as cloud–radiation interactions, air mass transport, and aqueous-phase chemistry (Liu et al., 2025; Luo et al., 2025).

Dependence analysis further quantifies the effects of varying input features on O_3 levels ***(Figure S6-S8)***. Relative humidity was determined to be the key feature at mountain foot. Specifically, O_3 concentrations exhibited a nonlinear inverse relationship with relative humidity, with notably enhanced O_3 levels under low- relative humidity conditions. Substantially elevated SHAP values further confirmed this relationship when relative humidity fell below approximately 80% at mountain foot ***(Figure S6A)***, and below 90% at both mountainside ***(Figure S7B)*** and mountaintop ***(Figure S8B)***. The relative humidity threshold for O_3 perturbation identified in this study was substantially higher than values reported for Hangzhou (~70%) (Zhang et al., 2024b) and Nanjing (~75%) (Zhang et al., 2024a). As relative humidity increased from 60% to 80%, the corresponding SHAP value diminished from approximately 15 ppb to near zero, indicating a reduction in the influence of relative humidity on O_3 concentration of ~15 ppb at mountain foot, which was approximately twofold higher than that reported in Haikou (~7.5 ppb) (Liu et al., 2025). At higher elevations (mountainside and mountaintop), the same relative humidity increase resulted in a smaller SHAP value decrease, from ~10 ppb to ~5 ppb, corresponding to an influence reduction of ~5 ppb, which remained lower than those recorded. This negative correlation was attributable primarily to the suppression of O_3 formation under elevated RH, which reduced air temperature, shortened peroxy radical chain lengths, diminished NO_2 cycling via aerosol liquid water enhancement, and catalytically destroyed existing O_3 through vapor-phase hydrolysis (Qiu et al., 2025; Yu, 2019; Zhang et al., 2024b; Zhang et al., 2024a). Temperature emerged as the predominant feature at both mountainside and mountaintop, with a notable nonlinear negative correlation ***(Figure S7A and S8A)***. Temperature exhibited threshold-and elevation-dependent effects on O_3 concentration variations, with critical thresholds of 20 °C ***(Figure S6D)***, 18 °C ***(Figure S7A)***, and 15 °C ***(Figure S8A)*** at mountain foot, mountainside, and mountaintop, respectively. This contrasted with positive temperature-O_3 correlations in urban plains, underscoring the critical role of mountain-specific processes (e.g., valley winds and cloud shading) in modulating O_3 dynamics. Wind speed and direction, collectively explained 21.3% of the O_3 concentration variability at mountaintop, exceeding their explanatory power at mountain foot and mountainside. Particularly, prevailing westerly winds (270°± 30°) consistently elevated O_3 levels (positive SHAP values), whereas easterly flows (90° ± 30°) suppressed concentrations. This distinct pattern stems from divergent air mass origins: westerlies transported dry, warm air masses enriched with anthropogenic precursors from the industrialized regions of Guizhou, while easterlies originated from the cleaner Wuling Mountains, thereby inhibiting photochemical O_3 production.

Regarding precursor species, O_3 variability was governed predominantly by NO_x at mountain foot, whereas at mountainside and mountaintop, O_3 levels were regulated primarily by VOCs species. Situated within the direct influence zone of near-ground pollution sources, the mountain foot site exhibits elevated NO_x emissions and consequently high atmospheric NO_x concentrations. These increased NO_x levels directly deplete O_3 through titration. Concurrently, high NO_x concentrations

https://doi.org/10.5194/egusphere-2025-4818
Preprint. Discussion started: 5 November 2025

promote the conversion of peroxy radicals to nitrate, thereby suppressing O_3 production. Consequently, variations in NO_x concentration-particularly the titration effect of NO-play a major role in driving the observed O_3 concentration variability. However, with increasing elevation, anthropogenic NO_x emissions intensity diminishes markedly. Concurrently, specific VOCs-reactive precursors and their oxidation products-influenced by enhanced biogenic emissions and transport-can exhibit greater efficiency for O_3 production under low-NO_x conditions. In brief, this systematic shift in precursor contribution with increasing elevation fundamentally reflects the dynamics shaped by photochemical regimes, source-sink distribution patterns, boundary layer physics, and key meteorological drivers within complex mountainous terrain.

3.3 Unveiling the O_3 formation mechanism

Reaction rates substantially influencing O_3 production or destruction are summarized in **Table 1** on a daily average basis. O_3 production rates peaked at mountain foot (12.83 ppb hr^{-1}), significantly exceeding values observed at mountainside (2.29 ppb hr^{-1}) and mountaintop (2.92 ppb hr^{-1}). This vertical gradient arises primarily from variations in NO concentrations, with significantly higher NO emission intensities at mountain foot-driven by anthropogenic activities-compared to mountainside and mountaintop. Elevated NO concentrations accelerate HO_2 and RO_2 reactions with NO, thereby promoting radical cycling rates and consequently amplifying O_3 production (Wu et al., 2024; Ma et al., 2002). The HO_2 + NO reaction dominated O_3 production pathways across all sites, with mean rates of 6.09 ppb hr^{-1} (47.5%), 1.23 ppb hr^{-1} (53.8%), and 1.48 ppb hr^{-1} (50.8%) at mountain foot, mountainside and mountaintop, respectively. The RO_2 + NO and CH_3O_2 + NO reactions constituted the secondary pathways. Corresponding mean rates were 3.80 and 2.94 ppb hr^{-1} (29.6% and 22.9%) at mountain foot, 0.71 and 0.35 ppb hr^{-1} (31.1% and 15.1%) at mountainside, and 0.98 and 0.46 ppb hr^{-1} (33.4% and 15.8%) at mountaintop. The O_3 removal rate reached 14.77 ppb h^{-1} at mountain foot, significantly higher than rates observed at mountainside (1.94 ppb h^{-1}) and mountaintop (2.64 ppb h^{-1}) ***(Table 1)***. The dominant removal pathway at mountain foot was the reaction of O_3 with NO_2 (7.14 ppb h^{-1}), accounting for 48.3% of the total removal. This was followed by reactions with 2-Butene (2.79 ppb h^{-1}, 18.9%) and photolysis (O_3 + hν, 1.36 ppb h^{-1}, 9.2%). In marked contrast, O_3 + hν was the primary removal mechanism at both mountainside and mountaintop, with mean daily rates of 0.43 ppb h^{-1} (22.3%) and 0.54 ppb h^{-1} (20.4%), respectively. Secondary pathways included O_3 + NO_2 (0.36 ppb h^{-1}, 18.4% at mountainside; 0.43 ppb h^{-1}, 16.3% at mountaintop) and O_3 + 1,2-Dimethylethylene (0.32 ppb h^{-1}, 16.4% at mountainside; 0.38 ppb h^{-1}, 14.5% at mountaintop). This vertical variation is primarily attributed to altitudinal gradients in meteorological parameters (temperature, and solar irradiation) and precursor concentrations. Figure 8 depicts the campaign-mean diurnal cycle of O_3 production, destruction, and net rates at mountain foot, mountainside, and mountaintop. One can see that both O_3 production and destruction occur concurrently during the daytime, peaking around solar noon. At mountain foot, O_3 destruction exceeded production, resulting in net O_3 destruction with a rate of 1.93 ppb hr^{-1} ***(Figure 6A and Table 1)***, contrasting with net O_3 production at mountainside (0.35 ppb hr^{-1}) ***(Figure 6B and Table 1)*** and mountaintop (0.29 ppb hr^{-1}) ***(Figure 6C and Table 1)***. These values were significantly lower than those recorded at Mount Tai (7.4 ppb hr^{-1} at mountain foot, 5.6 ppb hr^{-1} at mountainside and 6.4 ppb hr^{-1} at mountaintop)(Kanaya et al., 2009; Wu et al., 2024), comparable to measurements at Jungfraujoch for midday in winter, spring, and summer (from −0.05 to +0.4 ppb hr^{-1})(Parker et al., 2009; Zanis et al., 2003), but substantially higher than the data obtained from Mt. Cimone in June (2-3 ppb d^{-1})(Fischer et al., 2003) and Mauna Loa for four seasons (from −0.8 to −0.4 ppb d^{-1}) (Cantrell et al., 1996). The peak net O_3 production at mountain foot occurred around 08:00 (4.4 ppb hr^{-1}), approximately 2-3 hours earlier than that observed at mountainside (3.4 ppb hr^{-1}) and mountaintop (7.3 ppb hr^{-1}), respectively. This temporal offset may be linked to differences in the timing of precursor accumulation driven by boundary-layer development and tourist activity.

To evaluate O_3 control strategies, we conducted a suite of sensitivity simulations quantifying responses of three O_3 metrics-daily maximum hourly concentration (MConc), daily maximum net production rate (ROM), and daily average net production rate (ROD)-to precursor emissions. Analysis of Empirical Kinetic Modeling Approach (EKMA) curves and relative incremental reactivity (RIR) revealed that O_3 formation at mountain foot foot, mountainside, and mountaintop was predominantly NO_x-limited ***(Figure 7)***, with corresponding RIR values of 0.57, 0.83, and 0.78 ***(Figure 8A)***. However, a progressive shift towards increasing VOC sensitivity was observed with increasing altitude. RIR values for VOCs were -0.2,

https://doi.org/10.5194/egusphere-2025-4818
Preprint. Discussion started: 5 November 2025

0.42, and 0.55 at mountain foot, mountainside, and mountaintop, respectively, especially anthropogenic hydrocarbons-sensitive (RIR: -0.12–0.51), followed by reactive aromatics (-0.03–0.06) and alkenes (-0.04–0.04) ***(Figure 8B)***. This indicates that the availability and reactivity of anthropogenic hydrocarbons, reactive aromatics and alkenes become increasingly critical rate-limiting factors for O_3 production at higher elevations. Negative RIR values for VOCs at mountain foot indicated that O_3 formation is under a strong NO_x-limited regime, implying that VOCs reduction could paradoxically exacerbate O_3 pollution in this region. With increasing elevation, NO_x concentrations decreased more rapidly due to greater distance from emission sources and enhanced dilution. On the sensitivity curve, as NO_x concentrations decline to a certain level, variations in VOCs concentrations exert a proportionally greater influence on the O_3 formation, even when the system remains predominantly within the NO_x-limited regime. This finding underscores the necessity of accounting for spatial heterogeneity in atmospheric chemical processes induced by elevation when evaluating O_3 pollution control strategies in complex terrains, such as high mountains. While lower elevations remain primarily NO_x-controlled, higher elevations exhibit transitional characteristics marked by enhanced VOCs sensitivity. Consequently, implementing altitude-specific precursor reduction strategies-either differentiated or coordinated controls targeting both NO_x and specific VOCs-may prove more effective than uniform regional mitigation measures.

The variations in O_3 mixing ratios are governed predominantly by chemical and physical processes. As depicted in **Figure 9**, a distinct altitudinal gradient in O_3 transport dynamics occurred. During daytime, net O_3 transport at mountain foot was characterized by predominantly inward (convergent) fluxes, which contributed to the accumulation of observed daytime O_3 concentration ***(Figure 9A)***. This suggests that the foothill area acts as a receptor for O_3 or its precursors, likely influenced by upslope flows advecting air masses from the surrounding lower terrain or valley regions. CWT analysis revealed that O_3 influx predominantly occurs via northeasterly transport pathways ***(Figure S9A)***, while precursor species are primarily influenced by southwesterly advective transport ***(Figure S9B-D)***. Conversely, at mountainside and mountaintop, the dominant pattern shifts to outward (divergent) fluxes of O_3, which resulted in slight daytime O_3 decreases at these elevations ***(Figure 9B-C)***. This signifies that these higher elevation sites function as net sources of O_3 within the local atmospheric column during the day. The efflux is potentially driven by several factors: 1) intensified turbulent mixing and venting within the mountain boundary layer facilitating vertical export, 2) horizontal advection away from the mountain peak by prevailing winds aloft, and/or 3) local photochemical production exceeding titration or deposition losses at these altitudes under strong solar insolation. This vertical divergence in O_3 transport regimes-convergence at the base and divergence aloft-highlights the complex interplay between mountain-induced meteorology (e.g., thermally driven circulations, boundary layer development), atmospheric mixing processes, and photochemistry in governing the spatial distribution and fate of O_3 in mountainous terrain.

4 Conclusions and implications

Based on comprehensive vertical gradient observations and modeling analyses at Mount Fanjing, this study elucidates the characteristics and governing mechanisms of O_3 and its precursors in the high-altitude background atmosphere of the Yunnan–Guizhou Plateau. The results reveal a pronounced positive altitudinal gradient in O_3 concentrations, with values of 14.8 ± 15.2 ppb at 550 m, 30.4 ± 13.4 ppb at 1774 m, and 40.2 ± 14.7 ppb at 2119 m, contrasting with the decreasing trends of precursors such as VOCs, NO_x, and CO. A clear shift in the dominant factors controlling O_3 variability was observed along the elevation gradient. At the mountain foot, O_3 levels were governed mainly by NO_x and RH, with high RH (>80%) suppressing O_3 through lowered temperatures, shortened radical chain lengths, and enhanced aqueous-phase loss. In contrast, temperature and VOCs species became the primary drivers at the mountainside and summit.

O_3 formation regimes also exhibited elevation dependence. Net O_3 destruction prevailed at the mountain foot (-1.93 ppb hr^{-1}), dominated by O_3+NO_2 reactions (48.3% of loss). Conversely, the mountainside and mountaintop showed net production (+0.35 and +0.29 ppb hr^{-1}), primarily through HO_2/RO_2+NO reactions (>80% of production), with photolysis as the major loss pathway. Chemically, all elevations fell under NO_x-limited conditions, but VOCs sensitivity increased with altitude, with anthropogenic hydrocarbons dominating VOCs reactivity aloft, underscoring their growing importance under low-NOx conditions. Transport mechanisms further shaped O_3 distribution: daytime convergent flow at lower elevations imported O_3

https://doi.org/10.5194/egusphere-2025-4818
Preprint. Discussion started: 5 November 2025

and precursors via northeasterly winds, while divergent fluxes at higher levels exported O_3 from the mountainside and summit due to turbulent venting and advection. These patterns highlight the critical role of mountain-induced meteorology in regional O_3 dynamics. Our findings underscore the necessity of altitude-specific O_3 mitigation strategies and advocate for expanded high-altitude monitoring to better represent regional background pollution in understudied areas.

Data availability

The datasets generated and/or analyzed during this study, including those underpinning the main figures and supplementary information, are available at https://doi.org/10.5281/zenodo.17239121, Yang et al., (2025).

CRediT authorship contribution statement

Y.Y., H.Z and Y.H.W. conceived and designed the study. Y.Y., H.H, Y.H.W., H.B.L, and X.W.H. conducted the experimental measurements. Y.Y. and H.Z. analyzed the data and drafted the manuscript. H.Z., Z.Y, and Y.Y. performed the box model simulations. All authors contributed to the interpretation of the findings and provided critical feedback on the manuscript.

Competing interests

The authors declare no competing interests, whether financial or non-financial, that could be perceived as influencing the work reported in this study.

Acknowledgement

All supplementary figures and tables referenced in this study are provided in the Supplementary Information. The authors gratefully acknowledge Nutech (China) Co.,Ltd. for providing three sets of Ntrace VsCMS6500 VOCs online monitoring systems. We also thank Jiangsu Skyray Instrument Co., Ltd. for supplying three sets of online analyzers for O_3, NO_x, and CO. Appreciation is extended to Guizhou Zhitan Yunqing Technology Co., Ltd. for their assistance with the construction of the observation station infrastructure. Finally, we acknowledge Tianjin Winner Technology Co., Ltd. for their technical support in the operation and maintenance of the gradient observation station.

Financial support

This work was supported by the National Natural Science Foundation of China (grant no. 42307149, no. 42567016 and no. 42205098) and the Science and Technology Program of Guizhou Province (grant no. Qian Kehe Support 2024 General 139).

References

Andreae, M. O., Acevedo, O. C., Araùjo, A., Artaxo, P., Barbosa, C. G. G., Barbosa, H. M. J., Brito, J., Carbone, S., Chi, X., Cintra, B. B. L., da Silva, N. F., Dias, N. L., Dias-Júnior, C. Q., Ditas, F., Ditz, R., Godoi, A. F. L., Godoi, R. H. M., Heimann, M., Hoffmann, T., Kesselmeier, J., Könemann, T., Krüger, M. L., Lavric, J. V., Manzi, A. O., Lopes, A. P., Martins, D. L., Mikhailov, E. F., Moran-Zuloaga, D., Nelson, B. W., Nölscher, A. C., Santos Nogueira, D., Piedade, M. T. F., Pöhlker, C., Pöschl, U., Quesada, C. A., Rizzo, L. V., Ro, C. U., Ruckteschler, N., Sá, L. D. A., de Oliveira Sá, M., Sales, C. B., dos Santos, R. M. N., Saturno, J., Schöngart, J., Sörgel, M., de Souza, C. M., de Souza, R. A. F., Su, H., Targhetta, N., Tóta, J., Trebs, I., Trumbore, S., van Eijck, A., Walter, D., Wang, Z., Weber, B., Williams, J., Winderlich, J., Wittmann, F., Wolff, S., and Yáñez-Serrano, A. M.: The Amazon Tall Tower Observatory (ATTO): overview of pilot measurements on ecosystem ecology, meteorology, trace gases, and aerosols, **Atmos. Chem. Phys.**, 15, 10723-10776, doi:10.5194/acp-15-10723-2015, 2015.

Atkinson, R. and Arey, J.: Atmospheric Degradation of Volatile Organic Compounds., **Chemical Reviews**, 103, 4605-4638, doi:10.102/cr0206420, 2003.

Breiman, L.: Random Forests, **Machine Learning**, 45, 5-32, doi:10.1023/A:1010933404324, 2001.

Cantrell, C. A., Shetter, R. E., Gilpin, T. M., Calvert, J. G., Eisele, F. L., and Tanner, D. J.: Peroxy radical concentrations

https://doi.org/10.5194/egusphere-2025-4818
Preprint. Discussion started: 5 November 2025

measured and calculated from trace gas measurements in the Mauna Loa Observatory Photochemistry Experiment 2, **Journal of Geophysical Research: Atmospheres**, 101, 14653-14664, doi:10.1029/95JD03613, 1996.

Carter, W. P. L.: Development of Ozone Reactivity Scales for Volatile Organic Compounds, **Journal of the Air and Waste Management Association**, 44, 881-899, doi:10.1080/1073161x.1994.10467290, 2012.

Chen, C., Chen, W., Guo, L., Wu, Y., Duan, X., Wang, X., and Shao, M.: A comprehensive review of tropospheric background ozone: Definitions, estimation methods, and meta-analysis of its spatiotemporal distribution in China, **EGUsphere**, 2025, 1-59, doi:10.5194/egusphere-2025-687, 2025.

Chen, T., Xue, L., Zheng, P., Zhang, Y., Liu, Y., Sun, J., Han, G., Li, H., Zhang, X., Li, Y., Li, H., Dong, C., Xu, F., Zhang, Q., and Wang, W.: Volatile organic compounds and ozone air pollution in an oil production region in northern China, **Atmos. Chem. Phys.**, 20, 7069-7086, doi:10.5194/acp-20-7069-2020, 2020.

Cooper, O. R., Schultz, M. G., Schröder, S., Chang, K.-L., Gaudel, A., Benítez, G. C., Cuevas, E., Fröhlich, M., Galbally, I. E., Molloy, S., Kubistin, D., Lu, X., McClure-Begley, A., Nédélec, P., O'Brien, J., Oltmans, S. J., Petropavlovskikh, I., Ries, L., Senik, I., Sjöberg, K., Solberg, S., Spain, G. T., Spangl, W., Steinbacher, M., Tarasick, D., Thouret, V., and Xu, X.: Multi-decadal surface ozone trends at globally distributed remote locations, **Elementa: Science of the Anthropocene**, 8, doi:10.1525/elementa.420, 2020.

Dieu Hien, V. T., Lin, C., Thanh, V. C., Kim Oanh, N. T., Thanh, B. X., Weng, C.-E., Yuan, C.-S., and Rene, E. R.: An overview of the development of vertical sampling technologies for ambient volatile organic compounds (VOCs), **J Environ Manage**, 247, 401-412, doi:10.1016/j.jenvman.2019.06.090, 2019.

Feng, Z., Hu, E., Wang, X., Jiang, L., and Liu, X.: Ground-level O3 pollution and its impacts on food crops in China: A review, **Environ Pollut**, 199, 42-48, doi:10.1016/j.envpol.2015.01.016, 2015.

Feng, Z., Xu, Y., Kobayashi, K., Dai, L., Zhang, T., Agathokleous, E., Calatayud, V., Paoletti, E., Mukherjee, A., Agrawal, M., Park, R. J., Oak, Y. J., and Yue, X.: Ozone pollution threatens the production of major staple crops in East Asia, **Nature Food**, 3, 47-56, doi:10.1038/s43016-021-00422-6, 2022.

Fischer, H., Kormann, R., Klüpfel, T., Gurk, C., Königstedt, R., Parchatka, U., Mühle, J., Rhee, T. S., Brenninkmeijer, C. A. M., Bonasoni, P., and Stohl, A.: Ozone production and trace gas correlations during the June 2000 MINATROC intensive measurement campaign at Mt. Cimone, **Atmos. Chem. Phys.**, 3, 725-738, doi:10.5194/acp-3-725-2003, 2003.

Gao, J., Zhu, B., Xiao, H., Kang, H., Hou, X., Yin, Y., Zhang, L., and Miao, Q.: Diurnal variations and source apportionment of ozone at the summit of Mount Huang, a rural site in Eastern China, **Environ Pollut**, 222, 513-522, doi:10.1016/j.envpol.2016.11.031, 2017.

Gaudel, A., Cooper, O. R., Chang, K.-L., Bourgeois, I., Ziemke, J. R., Strode, S. A., Oman, L. D., Sellitto, P., Nédélec, P., Blot, R., Thouret, V., and Granier, C.: Aircraft observations since the 1990s reveal increases of tropospheric ozone at multiple locations across the Northern Hemisphere, **Science Advances**, 6, eaba8272, doi:10.1126/sciadv.aba8272, 2020.

Gong, D., Wang, H., Zhang, S., Wang, Y., Liu, S. C., Guo, H., Shao, M., He, C., Chen, D., He, L., Zhou, L., Morawska, L., Zhang, Y., and Wang, B.: Low-level summertime isoprene observed at a forested mountaintop site in southern China: implications for strong regional atmospheric oxidative capacity, **Atmos. Chem. Phys.**, 18, 14417-14432, doi:10.5194/acp-18-14417-2018, 2018.

https://doi.org/10.5194/egusphere-2025-4818
Preprint. Discussion started: 5 November 2025

Guo, H., Ling, Z. H., Cheng, H. R., Simpson, I. J., Lyu, X. P., Wang, X. M., Shao, M., Lu, H. X., Ayoko, G., Zhang, Y. L., Saunders, S. M., Lam, S. H. M., Wang, J. L., and Blake, D. R.: Tropospheric volatile organic compounds in China, **Sci Total Environ**, 574, 1021-1043, doi:10.1016/j.scitotenv.2016.09.116, 2017.

He, G., He, C., Wang, H., Lu, X., Pei, C., Qiu, X., Liu, C., Wang, Y., Liu, N., Zhang, J., Lei, L., Liu, Y., Wang, H., Deng, T., Fan, Q., and Fan, S.: Nighttime ozone in the lower boundary layer: insights from 3-year tower-based measurements in South China and regional air quality modeling, **Atmos. Chem. Phys.**, 23, 13107-13124, doi:10.5194/acp-23-13107-2023, 2023.

Jain, V., Tripathi, N., Tripathi, S. N., Gupta, M., Sahu, L. K., Murari, V., Gaddamidi, S., Shukla, A. K., and Prevot, A. S. H.: Real-time measurements of non-methane volatile organic compounds in the central Indo-Gangetic basin, Lucknow, India: source characterisation and their role in O3 and secondary organic aerosol formation, **Atmos. Chem. Phys.**, 23, 3383-3408, doi:10.5194/acp-23-3383-2023, 2023.

Kanaya, Y., Pochanart, P., Liu, Y., Li, J., Tanimoto, H., Kato, S., Suthawaree, J., Inomata, S., Taketani, F., Okuzawa, K., Kawamura, K., Akimoto, H., and Wang, Z. F.: Rates and regimes of photochemical ozone production over Central East China in June 2006: a box model analysis using comprehensive measurements of ozone precursors, **Atmos. Chem. Phys.**, 9, 7711-7723, doi:10.5194/acp-9-7711-2009, 2009.

Kanaya, Y., Akimoto, H., Wang, Z. F., Pochanart, P., Kawamura, K., Liu, Y., Li, J., Komazaki, Y., Irie, H., Pan, X. L., Taketani, F., Yamaji, K., Tanimoto, H., Inomata, S., Kato, S., Suthawaree, J., Okuzawa, K., Wang, G., Aggarwal, S. G., Fu, P. Q., Wang, T., Gao, J., Wang, Y., and Zhuang, G.: Overview of the Mount Tai Experiment (MTX2006) in central East China in June 2006: studies of significant regional air pollution, **Atmos. Chem. Phys.**, 13, 8265-8283, doi:10.5194/acp-13-8265-2013, 2013.

Li, J., Wang, Z., Akimoto, H., Gao, C., Pochanart, P., and Wang, X.: Modeling study of ozone seasonal cycle in lower troposphere over east Asia, **Journal of Geophysical Research: Atmospheres**, 112, doi:10.1029/2006JD008209, 2007.

Li, J., Zhu, C., Chen, H., Zhao, D., Xue, L., Wang, X., Li, H., Liu, P., Liu, J., Zhang, C., Mu, Y., Zhang, W., Zhang, L., Herrmann, H., Li, K., Liu, M., and Chen, J.: The evolution of cloud and aerosol microphysics at the summit of Mt. Tai, China, **Atmos. Chem. Phys.**, 20, 13735-13751, doi:10.5194/acp-20-13735-2020, 2020.

Li, X. B., Yuan, B., Wang, S., Wang, C., Lan, J., Liu, Z., Song, Y., He, X., Huangfu, Y., Pei, C., Cheng, P., Yang, S., Qi, J., Wu, C., Huang, S., You, Y., Chang, M., Zheng, H., Yang, W., Wang, X., and Shao, M.: Variations and sources of volatile organic compounds (VOCs) in urban region: insights from measurements on a tall tower, **Atmos. Chem. Phys.**, 22, 10567-10587, doi:10.5194/acp-22-10567-2022, 2022.

Liu, H., Meigen, Z., and and Han, X.: A review of surface ozone source apportionment in China, **Atmospheric and Oceanic Science Letters**, 13, 470-484, doi:10.1080/16742834.2020.1768025, 2020.

Liu, J., Chen, M., Chu, B., Chen, T., Ma, Q., Wang, Y., Zhang, P., Li, H., Zhao, B., Xie, R., Huang, Q., Wang, S., and He, H.: Assessing the Significance of Regional Transport in Ozone Pollution through Machine Learning: A Case Study of Hainan Island, **ACS ES&T Air**, 2, 416-425, doi:10.1021/acsestair.4c00297, 2025.

Liu, T., Hong, Y., Li, M., Xu, L., Chen, J., Bian, Y., Yang, C., Dan, Y., Zhang, Y., Xue, L., Zhao, M., Huang, Z., and Wang, H.: Atmospheric oxidation capacity and ozone pollution mechanism in a coastal city of southeastern China: analysis of a typical photochemical episode by an observation-based model, **Atmos. Chem. Phys.**, 22, 2173-2190, doi:10.5194/acp-22-2173-2022, 2022.

https://doi.org/10.5194/egusphere-2025-4818
Preprint. Discussion started: 5 November 2025

Lu, H., Lyu, X., Cheng, H., Ling, Z., and Guo, H.: Overview on the spatial-temporal characteristics of the ozone formation regime in China, **Environ Sci-Proc Imp**, 21, 916-929, doi:10.1039/c9em00098d, 2019.

Lundberg, S. M., Erion, G., Chen, H., DeGrave, A., Prutkin, J. M., Nair, B., Katz, R., Himmelfarb, J., Bansal, N., and Lee, S.-I.: From local explanations to global understanding with explainable AI for trees, **Nature Machine Intelligence**, 2, 56-67, doi:10.1038/s42256-019-0138-9, 2020.

Luo, Z., Peng, L., Lv, Z., He, T., Yi, W., Wang, Y., He, K., and Liu, H.: Impacts of shipping emissions on ozone pollution in China, **EGUsphere**, 2025, 1-18, doi:10.5194/egusphere-2025-2027, 2025.

Lyu, X., Guo, H., Zhang, W., Cheng, H., Yao, D., Lu, H., Zhang, L., Zeren, Y., Liu, X., Qian, Z., and Wang, S.: Ozone and its precursors in a high-elevation and highly forested region in central China: Origins, in-situ photochemistry and implications of regional transport, **Atmos Environ**, 259, 118540, doi:10.1016/j.atmosenv.2021.118540, 2021.

Ma, J., Tang, J., Zhou, X., and Zhang, X.: Estimates of the Chemical Budget for Ozone at Waliguan Observatory, **J Atmos Chem**, 41, 21-48, doi:10.1023/A:1013892308983, 2002.

Mo, Z., Huang, S., Yuan, B., Pei, C., Song, Q., Qi, J., Wang, M., Wang, B., Wang, C., and Shao, M.: Tower-based measurements of NMHCs and OVOCs in the Pearl River Delta: Vertical distribution, source analysis and chemical reactivity, **Environ Pollut**, 292, 118454, doi:10.1016/j.envpol.2021.118454, 2022.

Okamoto, S. and Tanimoto, H.: A review of atmospheric chemistry observations at mountain sites, **Progress in Earth and Planetary Science**, 3, doi:10.1186/s40645-016-0109-2, 2016.
Parker, A. E., Monks, P. S., Wyche, K. P., Balzani-Lööv, J. M., Staehelin, J., Reimann, S., Legreid, G., Vollmer, M. K., and Steinbacher, M.: Peroxy radicals in the summer free troposphere: seasonality and potential for heterogeneous loss, **Atmos. Chem. Phys.**, 9, 1989-2006, doi:10.5194/acp-9-1989-2009, 2009.

Qiu, Y., Li, X., Chai, W., Liu, Y., Song, M., Tian, X., Zou, Q., Lou, W., Zhang, W., Li, J., and Zhang, Y.: Insights into ozone pollution control in urban areas by decoupling meteorological factors based on machine learning, **Atmos. Chem. Phys.**, 25, 1749-1763, doi:10.5194/acp-25-1749-2025, 2025.

Seibert, P., Kromp-Kolb, H., Baltensperger, U., Jost, D. T., and Schwikowski, M.: Trajectory Analysis of High-Alpine Air Pollution Data, in: Air Pollution Modeling and Its Application X, edited by: Gryning, S.-E., and Millán, M. M., Springer US, Boston, MA, 595-596, doi:10.1007/978-1-4615-1817-4_65, 1994.

Shi, Z., Vu, T., Kotthaus, S., Harrison, R. M., Grimmond, S., Yue, S., Zhu, T., Lee, J., Han, Y., Demuzere, M., Dunmore, R. E., Ren, L., Liu, D., Wang, Y., Wild, O., Allan, J., Acton, W. J., Barlow, J., Barratt, B., Beddows, D., Bloss, W. J., Calzolai, G., Carruthers, D., Carslaw, D. C., Chan, Q., Chatzidiakou, L., Chen, Y., Crilley, L., Coe, H., Dai, T., Doherty, R., Duan, F., Fu, P., Ge, B., Ge, M., Guan, D., Hamilton, J. F., He, K., Heal, M., Heard, D., Hewitt, C. N., Hollaway, M., Hu, M., Ji, D., Jiang, X., Jones, R., Kalberer, M., Kelly, F. J., Kramer, L., Langford, B., Lin, C., Lewis, A. C., Li, J., Li, W., Liu, H., Liu, J., Loh, M., Lu, K., Lucarelli, F., Mann, G., McFiggans, G., Miller, M. R., Mills, G., Monk, P., Nemitz, E., O'Connor, F., Ouyang, B., Palmer, P. I., Percival, C., Popoola, O., Reeves, C., Rickard, A. R., Shao, L., Shi, G., Spracklen, D., Stevenson, D., Sun, Y., Sun, Z., Tao, S., Tong, S., Wang, Q., Wang, W., Wang, X., Wang, X., Wang, Z., Wei, L., Whalley, L., Wu, X., Wu, Z., Xie, P., Yang, F., Zhang, Q., Zhang, Y., Zhang, Y., and Zheng, M.: Introduction to Special Issue - In-depth study of air pollution sources and processes within Beijing and its surrounding region (APHH-Beijing), **Atmos. Chem. Phys.**, 19, 7519-7546, doi:10.5194/acp-19-7519-2019, 2019.

https://doi.org/10.5194/egusphere-2025-4818
Preprint. Discussion started: 5 November 2025

Shtabkin, Y. A., Moiseenko, K. B., Skorokhod, A. I., Berezina, E. V., and Vasileva, A. V.: Sources and variations of tropospheric ozone in central Siberia: observations and model simulations, **IOP Conference Series: Earth and Environmental Science**, 606, 012058, doi:10.1088/1755-1315/606/1/012058, 2020.

Sun, L., Xue, L., Wang, T., Gao, J., Ding, A., Cooper, O. R., Lin, M., Xu, P., Wang, Z., Wang, X., Wen, L., Zhu, Y., Chen, T., Yang, L., Wang, Y., Chen, J., and Wang, W.: Significant increase of summertime ozone at Mount Tai in Central Eastern China, **Atmos. Chem. Phys.**, 16, 10637-10650, doi:10.5194/acp-16-10637-2016, 2016.

Tan, Z., Lu, K., Jiang, M., Su, R., Wang, H., Lou, S., Fu, Q., Zhai, C., Tan, Q., Yue, D., Chen, D., Wang, Z., Xie, S., Zeng, L., and Zhang, Y.: Daytime atmospheric oxidation capacity in four Chinese megacities during the photochemically polluted season: a case study based on box model simulation, **Atmos Chem Phys**, 19, 3493-3513, doi:10.5194/acp-19-3493-2019, 2019.

Tong, M., Xu, H., Wang, R., Liu, H., Li, J., Li, P., Qiu, X., Gong, J., Shang, J., Zhu, T., and Xue, T.: Estimating birthweight reduction attributable to maternal ozone exposure in low- and middle-income countries, **Science Advances**, 9, eadh4363, doi:10.1126/sciadv.adh4363, 2023.

Wang, T., Xue, L., Brimblecombe, P., Lam, Y. F., Li, L., and Zhang, L.: Ozone pollution in China: A review of concentrations, meteorological influences, chemical precursors, and effects, **Sci Total Environ**, 575, 1582-1596, doi:10.1016/j.scitotenv.2016.10.081, 2017.

Wang, Y., Yao, N., Liu, Y., Li, S., Ma, P., Liao, Z., Ren, X., Li, S., Chu, B., Ma, Q., Xin, J., Ma, Y., Quan, J., and He, H.: Campaign for Direct In Situ Study of Residual Layer Chemistry in Urban Beijing, **B Am Meteorol Soc**, 106, E625-E641, doi:10.1175/BAMS-D-24-0127.1, 2025.

Wang, Y., Gao, W., Wang, S., Song, T., Gong, Z., Ji, D., Wang, L., Liu, Z., Tang, G., Huo, Y., Tian, S., Li, J., Li, M., Yang, Y., Chu, B., Petäjä, T., Kerminen, V.-M., He, H., Hao, J., Kulmala, M., Wang, Y., and Zhang, Y.: Contrasting trends of PM2.5 and surface-ozone concentrations in China from 2013 to 2017, **National Science Review**, 7, 1331-1339, doi:10.1093/nsr/nwaa032, 2020.

Wang, Y. H., Hu, B., Ji, D. S., Liu, Z. R., Tang, G. Q., Xin, J. Y., Zhang, H. X., Song, T., Wang, L. L., Gao, W. K., Wang, X. K., and Wang, Y. S.: Ozone weekend effects in the Beijing–Tianjin–Hebei metropolitan area, China, **Atmos Chem Phys**, 14, 2419-2429, doi:10.5194/acp-14-2419-2014, 2014.

Wang, Z., Li, J., Wang, X., Pochanart, P., and Akimoto, H.: Modeling of Regional High Ozone Episode Observed at Two Mountain Sites (Mt. Tai and Huang) in East China, **J Atmos Chem**, 55, 253-272, doi:10.1007/s10874-006-9038-6, 2006.

Wolfe, G. M., Marvin, M. R., Roberts, S. J., Travis, K. R., and Liao, J.: The Framework for 0-D Atmospheric Modeling (F0AM) v3.1, **Geosci. Model Dev.**, 9, 3309-3319, doi:10.5194/gmd-9-3309-2016, 2016.

Wu, C., Chen, Y., Sun, Y., Zhang, H., Zhang, S., Cao, C., Li, J., and Wang, G.: Effects of Anthropogenic Pollutants on Biogenic Secondary Organic Aerosol Formation in the Atmosphere of Mt. Hua, China, **EGUsphere**, 2025, 1-32, doi:10.5194/egusphere-2025-1668, 2025.

Wu, W., Ge, Y., Wang, Y., Su, J., Wang, X., Zhou, B., and Chen, J.: Vertical ozone formation mechanisms resulting from increased oxidation on the mountainside of Mount Tai, China, **PNAS Nexus**, 3, doi:10.1093/pnasnexus/pgae347, 2024.

https://doi.org/10.5194/egusphere-2025-4818
Preprint. Discussion started: 5 November 2025

Xing, C., Liu, C., Ye, C., Xue, J., Wu, H., Ji, X., Ou, J., and Hu, Q.: Observations of the vertical distributions of summertime atmospheric pollutants in Nam Co: OH production and source analysis, **Atmos. Chem. Phys.**, 24, 10093-10112, doi:10.5194/acp-24-10093-2024, 2024.

Xu, W., Lin, W., Xu, X., Tang, J., Huang, J., Wu, H., and Zhang, X.: Long-term trends of surface ozone and its influencing factors at the Mt Waliguan GAW station, China – Part 1: Overall trends and characteristics, **Atmos. Chem. Phys.**, 16, 6191-6205, doi:10.5194/acp-16-6191-2016, 2016.

Xue, C., Ye, C., Kleffmann, J., Zhang, W., He, X., Liu, P., Zhang, C., Zhao, X., Liu, C., Ma, Z., Liu, J., Wang, J., Lu, K., Catoire, V., Mellouki, A., and Mu, Y.: Atmospheric measurements at Mt. Tai – Part II: HONO budget and radical (ROx + NO3) chemistry in the lower boundary layer, **Atmos. Chem. Phys.**, 22, 1035-1057, doi:10.5194/acp-22-1035-2022, 2022.

Xue, L., Wang, T., Simpson, I. J., Ding, A., Gao, J., Blake, D. R., Wang, X., Wang, W., Lei, H., and Jin, D.: Vertical distributions of non-methane hydrocarbons and halocarbons in the lower troposphere over northeast China, **Atmos Environ**, 45, 6501-6509, doi:10.1016/j.atmosenv.2011.08.072, 2011a.

Xue, L. K., Wang, T., Guo, H., Blake, D. R., Tang, J., Zhang, X. C., Saunders, S. M., and Wang, W. X.: Sources and photochemistry of volatile organic compounds in the remote atmosphere of western China: results from the Mt. Waliguan Observatory, **Atmos. Chem. Phys.**, 13, 8551-8567, doi:10.5194/acp-13-8551-2013, 2013.

Xue, L. K., Wang, T., Gao, J., Ding, A. J., Zhou, X. H., Blake, D. R., Wang, X. F., Saunders, S. M., Fan, S. J., Zuo, H. C., Zhang, Q. Z., and Wang, W. X.: Ground-level ozone in four Chinese cities: precursors, regional transport and heterogeneous processes, **Atmos. Chem. Phys.**, 14, 13175-13188, doi:10.5194/acp-14-13175-2014, 2014.

Xue, L. K., Wang, T., Zhang, J. M., Zhang, X. C., Deliger, Poon, C. N., Ding, A. J., Zhou, X. H., Wu, W. S., Tang, J., Zhang, Q. Z., and Wang, W. X.: Source of surface ozone and reactive nitrogen speciation at Mount Waliguan in western China: New insights from the 2006 summer study, **Journal of Geophysical Research: Atmospheres**, 116, doi:10.1029/2010JD014735, 2011b.

Yang, X., Xue, L., Yao, L., Li, Q., Wen, L., Zhu, Y., Chen, T., Wang, X., Yang, L., Wang, T., Lee, S., Chen, J., and Wang, W.: Carbonyl compounds at Mount Tai in the North China Plain: Characteristics, sources, and effects on ozone formation, **Atmos Res**, 196, 53-61, doi:10.1016/j.atmosres.2017.06.005, 2017.

Yang, Y., Wang, Y., Zhou, P., Yao, D., Ji, D., Sun, J., Wang, Y., Zhao, S., Huang, W., Yang, S., Chen, D., Gao, W., Liu, Z., Hu, B., Zhang, R., Zeng, L., Ge, M., Petäjä, T., Kerminen, V. M., Kulmala, M., and Wang, Y.: Atmospheric reactivity and oxidation capacity during summer at a suburban site between Beijing and Tianjin, **Atmos Chem Phys**, 20, 8181-8200, doi:10.5194/acp-20-8181-2020, 2020.

Yang, Y., Li, H., Wang, Y., Zhang, H., Yang, Z., Hou, X., Yao, D., Hu, H., Zhu, K., Xiong, Y., Lai, L, Chen, D., and Feng, P.: Measurement report: Altitudinal Shift of Ozone Regimes in a Mountainous Background Region, [datasets], https://doi.org/10.5281/zenodo.17239121.

Yu, S.: Fog geoengineering to abate local ozone pollution at ground level by enhancing air moisture, **Environmental Chemistry Letters**, 17, 565-580, doi:10.1007/s10311-018-0809-5, 2019.

https://doi.org/10.5194/egusphere-2025-4818
Preprint. Discussion started: 5 November 2025

Zanis, P., Monks, P. S., Green, T. J., Schuepbach, E., Carpenter, L. J., Mills, G. P., Rickard, A. R., Brough, N., and Penkett, S. A.: Seasonal variation of peroxy radicals in the lower free troposphere based on observations from the FREE Tropospheric EXperiments in the Swiss Alps, **Geophys Res Lett**, 30, doi:10.1029/2003GL017122, 2003.

Zhang, C., Xie, Y., Shao, M., and Wang, Q.: Application of machine learning to analyze ozone sensitivity to influencing factors: A case study in Nanjing, China, **Sci Total Environ**, 929, 172544, doi:10.1016/j.scitotenv.2024.172544, 2024a.

Zhang, L., Wang, L., Ji, D., Xia, Z., Nan, P., Zhang, J., Li, K., Qi, B., Du, R., Sun, Y., Wang, Y., and Hu, B.: Explainable ensemble machine learning revealing the effect of meteorology and sources on ozone formation in megacity Hangzhou, China, **Sci Total Environ**, 922, 171295, doi:10.1016/j.scitotenv.2024.171295, 2024b.

Zhang, Y., Liu, Y., Ma, W., Hua, C., Zheng, F., Lian, C., Wang, W., Xia, M., Zhao, Z., Li, J., Xie, J., Wang, Z., Wang, Y., Chen, X., Zhang, Y., Feng, Z., Yan, C., Chu, B., Du, W., Kerminen, V. M., Bianchi, F., Petaja, T., Worsnop, D., and Kulmala, M.: Changing aerosol chemistry is redefining HONO sources, **Nat Commun**, 16, 5238, doi:10.1038/s41467-025-60614-7, 2025.

Zheng, H., Kong, S. F., Xing, X. L., Mao, Y., Hu, T. P., Ding, Y., Li, G., Liu, D. T., Li, S. L., and Qi, S. H.: Monitoring of volatile organic compounds (VOCs) from an oil and gas station in northwest China for 1 year, **Atmos Chem Phys**, 18, 4567-4595, doi:10.5194/acp-18-4567-2018, 2018.

Zheng, H., Kong, S., Wu, F., Cheng, Y., Niu, Z., Zheng, S., Yang, G., Yao, L., Yan, Q., Wu, J., Zheng, M., Chen, N., Xu, K., Yan, Y., Liu, D., Zhao, D., Zhao, T., Bai, Y., Li, S., and Qi, S.: Intra-regional transport of black carbon between the south edge of the North China Plain and central China during winter haze episodes, **Atmos Chem Phys**, 19, 4499-4516, doi:10.5194/acp-19-4499-2019, 2019.

Zhong, B., Jiang, B., Zhou, J., Zhang, T., Chen, D., Zhai, Y., Luo, J., Deng, M., Xiao, M., Jiang, J., Li, J., and Shao, M.: Why observed and modelled ozone production rates and sensitives differ, a case study at rural site in China, **EGUsphere**, 2025, 1-24, doi:10.5194/egusphere-2025-1618, 2025.

Zhou, J., Zhang, C., Liu, A., Yuan, B., Wang, Y., Wang, W., Zhou, J. P., Hao, Y., Li, X. B., He, X., Song, X., Chen, Y., Yang, S., Yang, S., Wu, Y., Jiang, B., Huang, S., Liu, J., Peng, Y., Qi, J., Deng, M., Zhong, B., Huangfu, Y., and Shao, M.: Measurement report: Vertical and temporal variability in the near-surface ozone production rate and sensitivity in an urban area in the Pearl River Delta region, China, **Atmos. Chem. Phys.**, 24, 9805-9826, doi:10.5194/acp-24-9805-2024, 2024.

Zhu, S., Zhou, M., Qiao, L., Huang, D. D., Wang, Q., Wang, S., Gao, Y., Jing, S., Wang, Q., Wang, H., Chen, C., Huang, C., and Yu, J. Z.: Evolution and chemical characteristics of organic aerosols during wintertime PM2.5 episodes in Shanghai, China: insights gained from online measurements of organic molecular markers, **Atmos. Chem. Phys.**, 23, 7551-7568, doi:10.5194/acp-23-7551-2023, 2023.

https://doi.org/10.5194/egusphere-2025-4818
Preprint. Discussion started: 5 November 2025

Figures

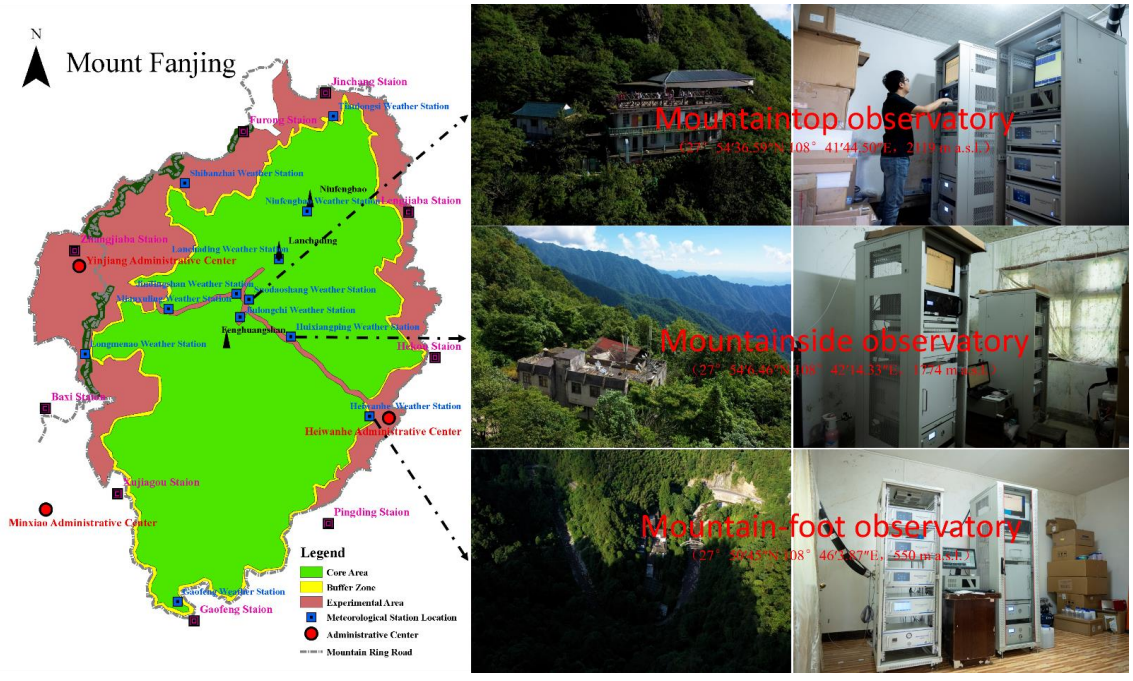

Figure 1. **Left panel**: Distribution of automatic weather stations within the core zone of the Fanjingshan National Nature Reserve. Numbers adjacent to stations denote elevation (image credit: Administration of Guizhou Fanjingshan National Nature Reserve). **Right panel**: External settings and instrumental configurations of O_3 and precursor monitoring stations at the mountain foot (Heiwanhe), mountainside (Huixiangping), and mountaintop (upper cable car station) (image credit: Colorful Guizhou, photographed on 24 July 2024).

https://doi.org/10.5194/egusphere-2025-4818
Preprint. Discussion started: 5 November 2025

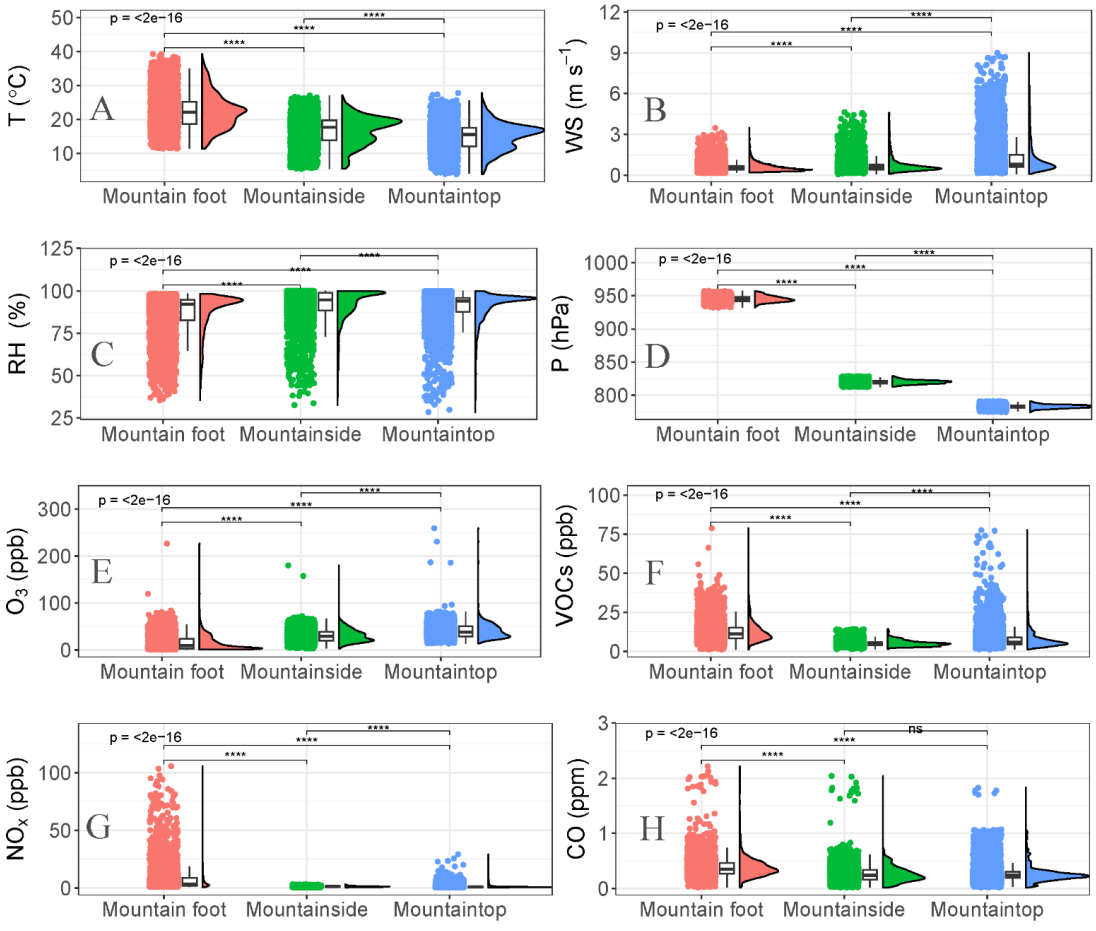

Figure 2. The comparatively visualize the distribution of O_3 and its precursors (VOCs, NO_x and CO) and meteorological parameters (ambient temperature (T) , wind speed(WS), relative humidity (RH) and atmospheric pressure (P)) at the mountain foot, mountainside and mountaintop. Each seasonal dataset is represented through four complementary graphical elements: 1. Right "cloud" component: A kernel density estimation illustrating the probability distribution of target species concentrations, highlighting seasonal variations in central tendency and dispersion; 2. Left "raindrop" component: Horizontally jittered data points depicting raw measurements, revealing underlying data density and distributional characteristics; 3. Central "boxplot" component: A Tukey-style boxplot summarizing key statistical descriptors, enabling robust inter-seasonal comparisons of distributional properties, with medians marked by black lines in the middle and the 25th and 75th percentiles as bounds. Whiskers extend to 1.5× the interquartile range; 4. Top "asterisk" component: The six-pointed star denoting the results of a kruskal.test assessing the statistical significance of differences between two interconnected datasets, ns: $p > 0.05$; *: $p <= 0.05$; **: $p <= 0.01$; ***: $p <= 0.001$; ****: $p <= 0.0001$.

https://doi.org/10.5194/egusphere-2025-4818
Preprint. Discussion started: 5 November 2025

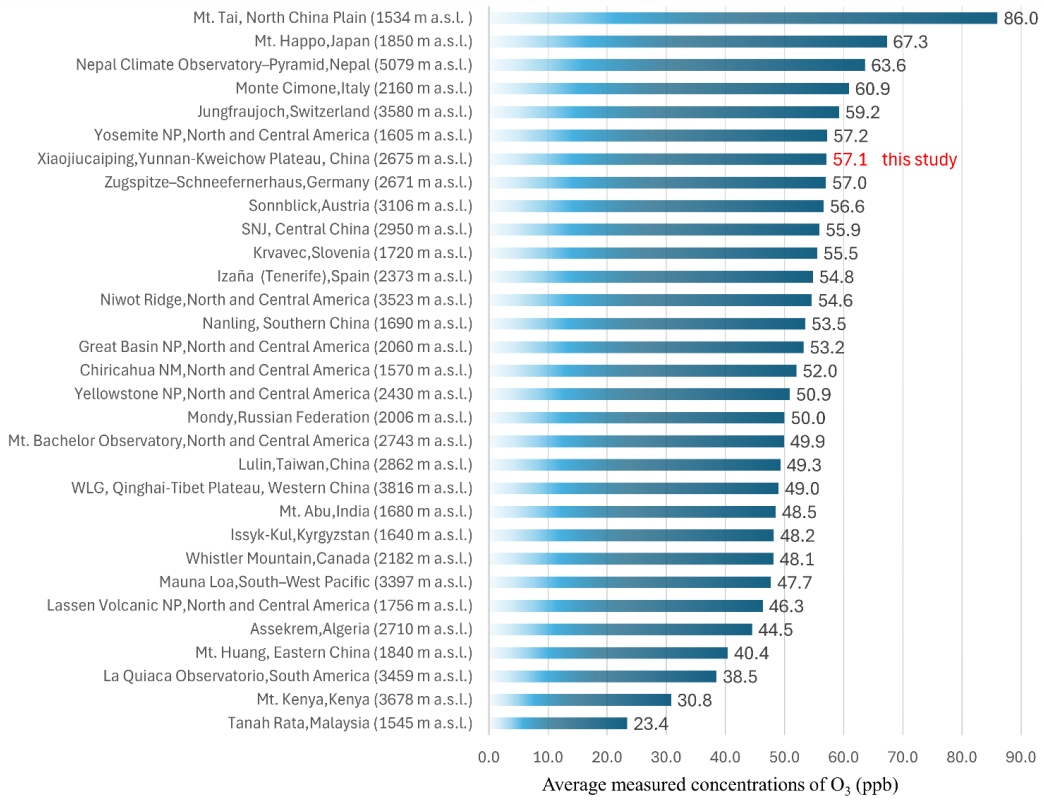

781

782 Figure 3. Comparison of O_3 concentrations at Mt. Fanjing summit with those observed at mountain sites across the globe. All
783 average values are reported in ppb. Data were compiled from published literature (Okamoto and Tanimoto, 2016; Li et al.,
784 2007; Lyu et al., 2021; Xu et al., 2016; Gong et al., 2018; Sun et al., 2016).

https://doi.org/10.5194/egusphere-2025-4818
Preprint. Discussion started: 5 November 2025

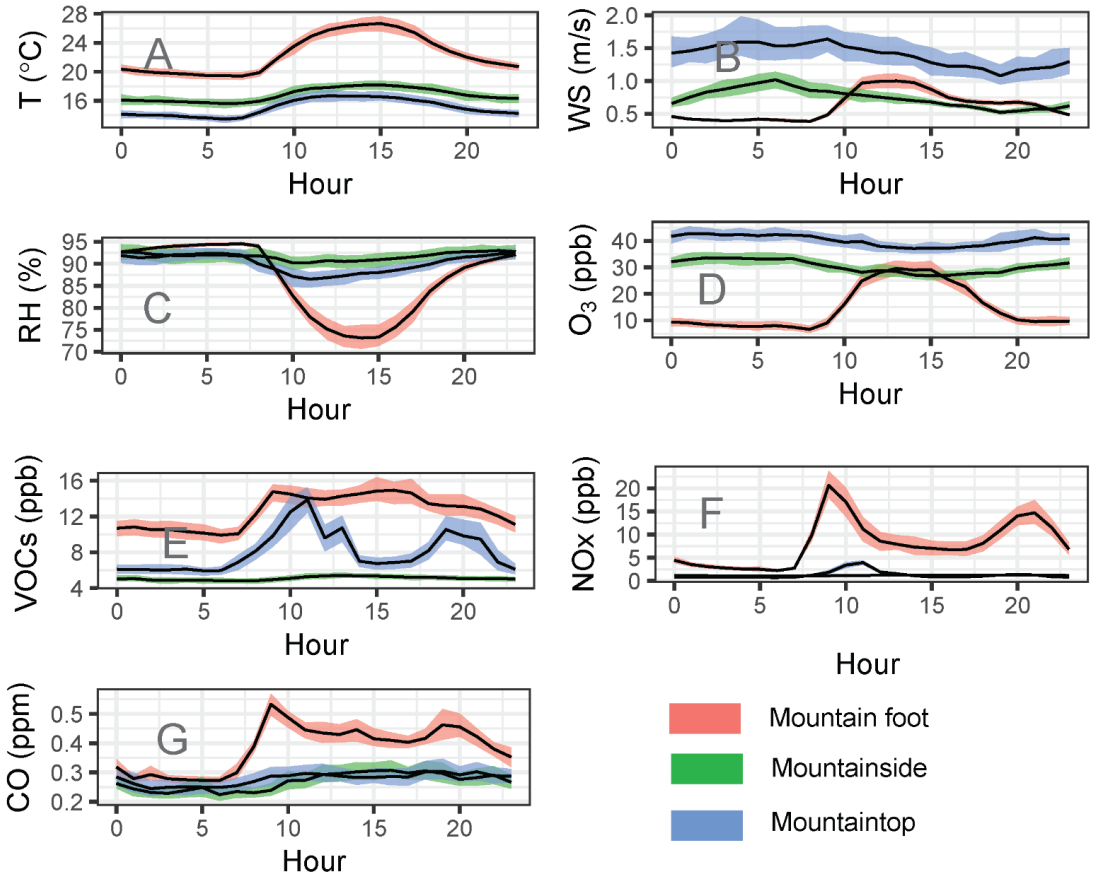

Figure 4. Diurnal variations in O_3 and its precursors, and meteorological parameters across the respective elevation sites throughout the observational period. Hourly means are represented by solid lines, with shaded areas denoting 95% confidence intervals.

https://doi.org/10.5194/egusphere-2025-4818
Preprint. Discussion started: 5 November 2025

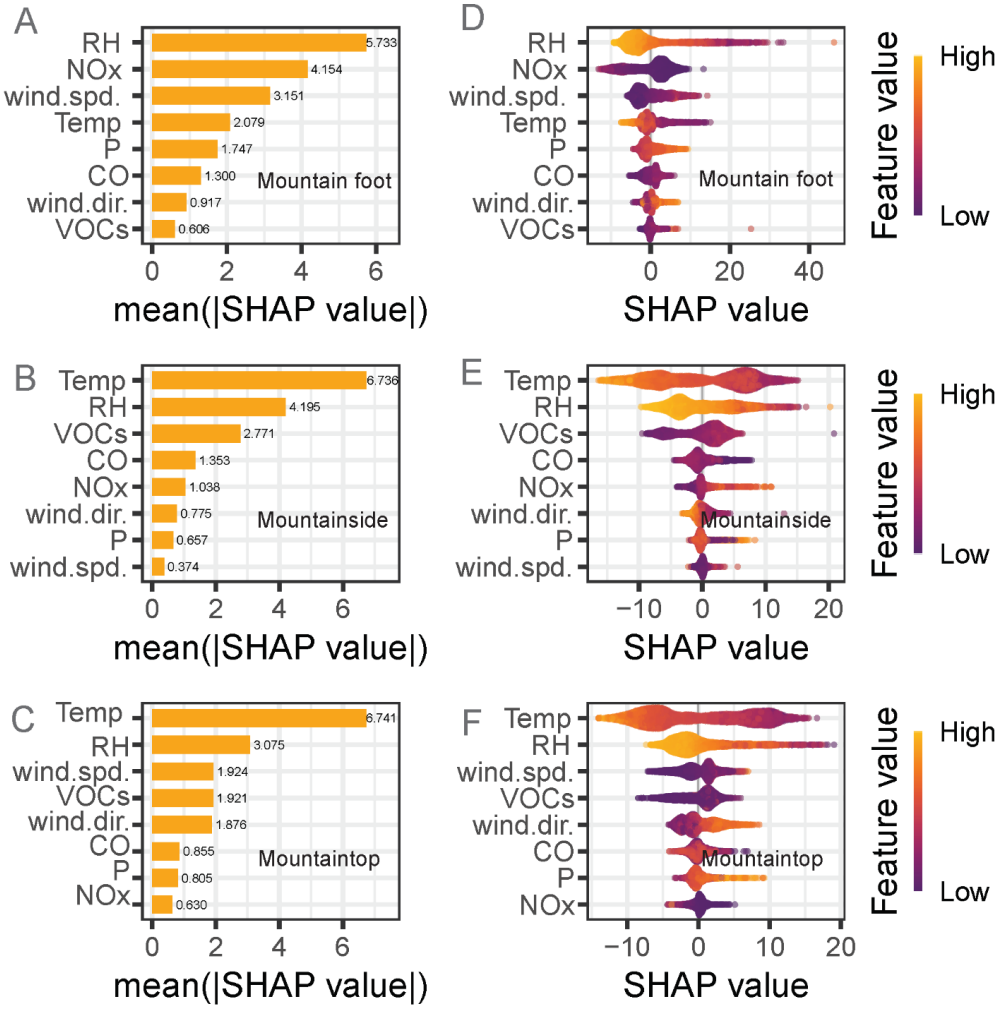

Figure 5. **A-C** The mean absolute SHAP (|SHAP|) values of the variables, computed using the SHapley Additive exPlanation (SHAP) method, quantify the relative importance of each feature in influencing O_3 concentrations within the random forest regression model at the respective elevation sites. The relative importance of each feature is quantified by computing the mean absolute SHAP value for each feature across the entire dataset. A higher mean absolute SHAP value indicates greater relative contribution of the corresponding feature to the model's predictions. **D-E** Feature importance analysis of the random forest regression model, with O_3 concentration as the dependent variable, was performed using the SHAP method across different elevation sites. In the summary plot, the absolute magnitude of a feature's SHAP value deviation from zero provides a robust metric for assessing its relative contribution to the model's predictive output. Positive SHAP values indicate features that positively influence the target variable, whereas negative values reflect inhibitory or adverse effects.

https://doi.org/10.5194/egusphere-2025-4818
Preprint. Discussion started: 5 November 2025

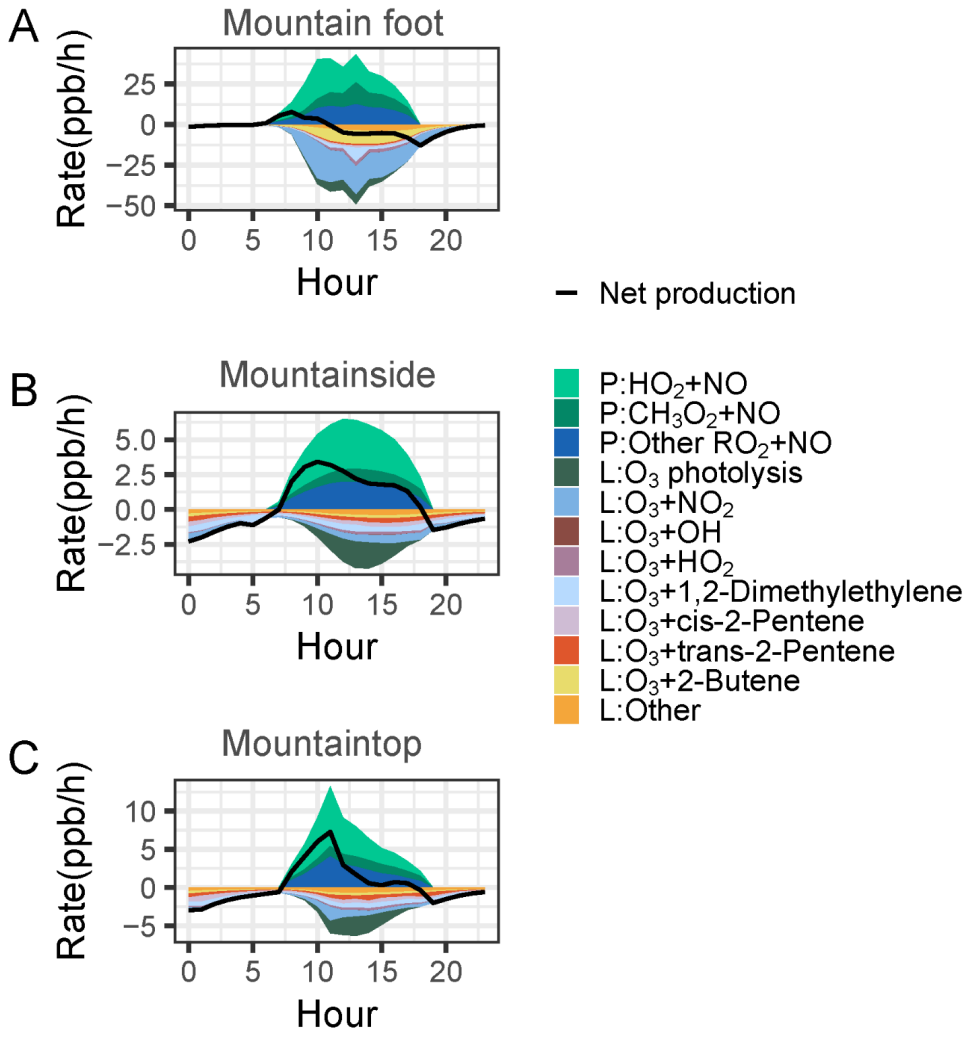

799

800 Figure 6. Mean diurnal profiles delineating the simulated contributions of individual pathways to O_3 production and
801 destruction rates are presented, accompanied by corresponding net O_3 production rates across altitudinal gradients.

https://doi.org/10.5194/egusphere-2025-4818
Preprint. Discussion started: 5 November 2025

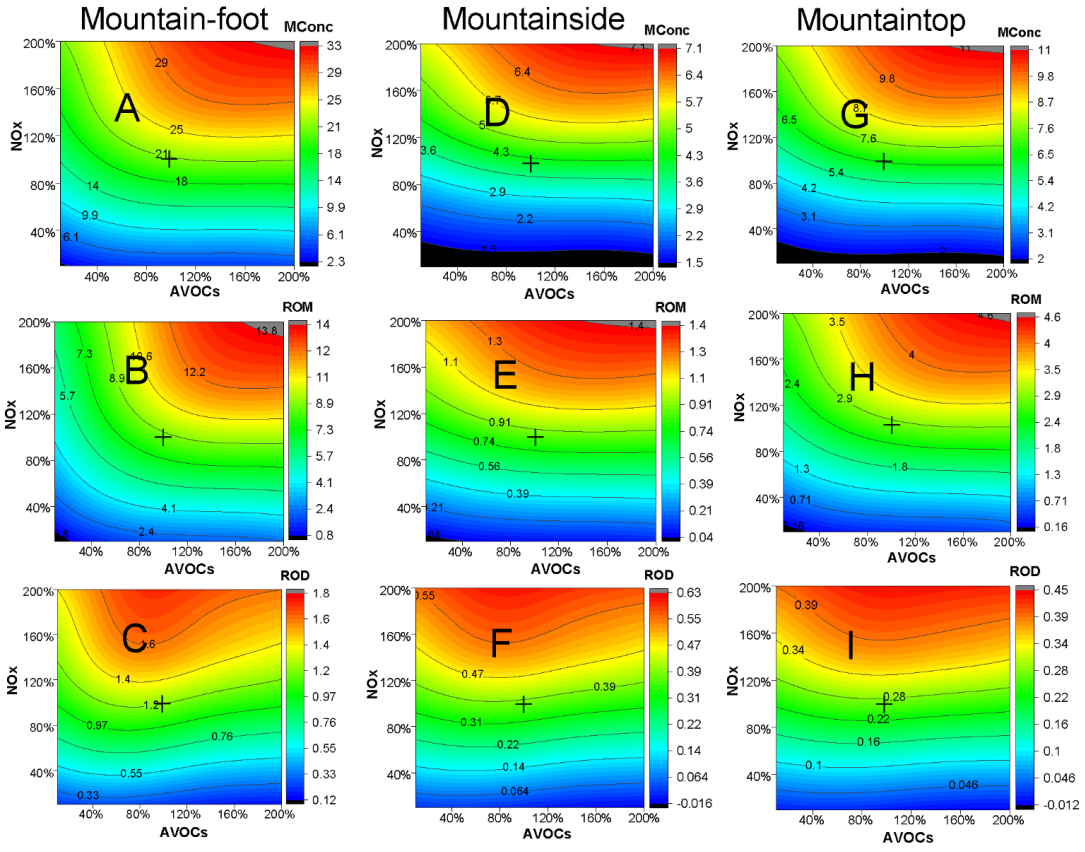

Figure 7. The isopleths of the daily maximum hourly O_3 concentration (MConc) (units: ppb), daily maximum net O_3 production rate (ROM) (units: ppb/h), and daily average net O_3 production rate (ROD) (units: ppb/h) as a function of the relative changes in anthropogenic VOCs (AVOCs) and NO_x across varying elevation sites during the entire observational period. The black cross represents at point 1,1 represents modelled Mconc, ROM and ROD at observed VOC and NO_x concentrations.

https://doi.org/10.5194/egusphere-2025-4818
Preprint. Discussion started: 5 November 2025

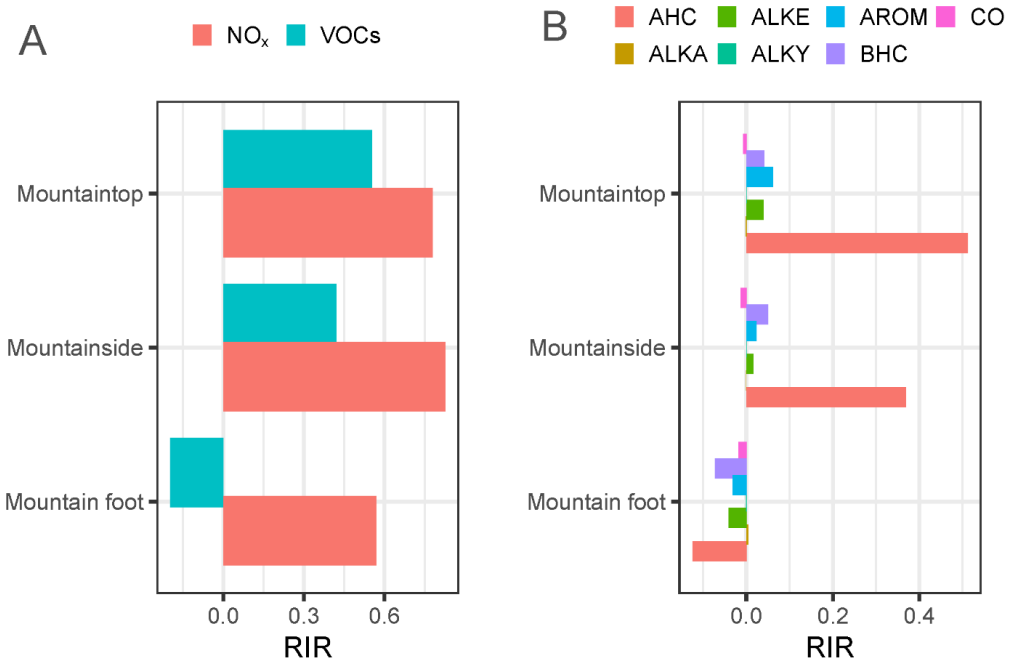

Figure 8. Model-calculated relative incremental reactivity (RIR) distributions for (A) major O_3 precursor groups and (B) VOCs sub-groups across altitudinal gradients during the observational campaign. Key to abbreviations: AHC, anthropogenic hydrocarbons; ALKA, alkanes; ALKE, alkenes; ALKY, acetylene; AROM, reactive aromatics; BHC, biogenic hydrocarbons.

https://doi.org/10.5194/egusphere-2025-4818
Preprint. Discussion started: 5 November 2025

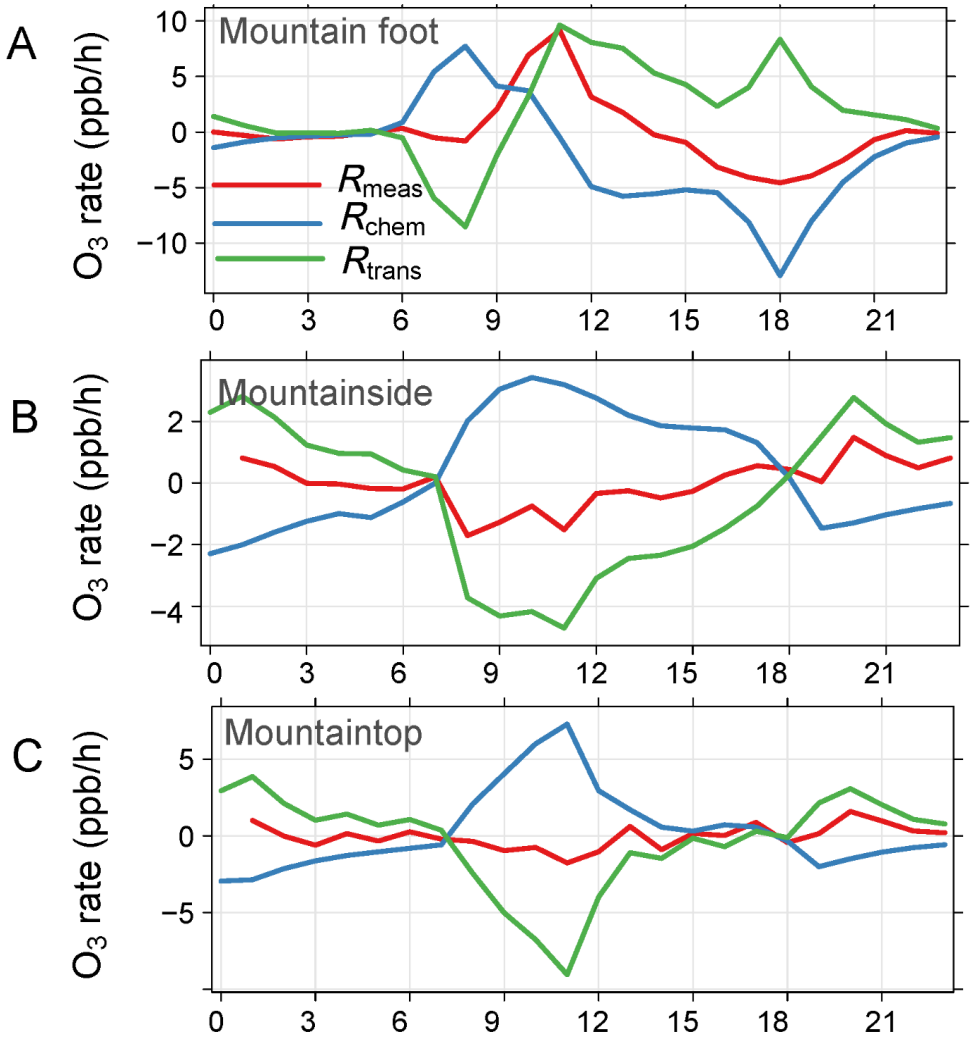

Figure 9. The accumulation of O_3 arises from both local photochemical production and regional transport processes across altitudinal gradients. In the legend, R_{chem}, R_{tran}, and R_{meas} denote the local O_3 photochemical production rate, regional transport contribution, and observed O_3 formation rate, respectively.

https://doi.org/10.5194/egusphere-2025-4818
Preprint. Discussion started: 5 November 2025

828

829 **Tables**

830 Table 1. Daily-averaged chemical reaction rates governing O_3 budget

Reaction	*Mountain foot*	*Mountainside*	*Mountaintop*
Production			
HO_2 + NO	6.09 (47.5%)	1.23 (53.8%)	1.48 (50.8%)
CH_3O_2 + NO	2.94 (22.9%)	0.35 (15.1%)	0.46 (15.8%)
RO_2 + NO	3.80 (29.6%)	0.71 (31.1%)	0.98 (33.4%)
Total	12.83	2.29	2.92
Destruction			
O_3+hv	1.36 (9.2%)	0.43 (22.3%)	0.54 (20.4%)
O_3+NO_2	7.14 (48.3%)	0.36 (18.4%)	0.43 (16.3%)
O_3+OH	0.02 (0.2%)	0.00 (0.2%)	0.00 (0.2%)
O_3+HO_2	0.58 (3.9%)	0.08 (4.2%)	0.12 (4.4%)
O_3+1,2-Dimethylethylene	0.93 (6.3%)	0.32 (16.4%)	0.38 (14.5%)
O_3+cis-2-Pentene	0.36 (2.5%)	0.20 (10.4%)	0.34 (12.7%)
O_3+trans-2-Pentene	0.36 (2.4%)	0.21 (11.0%)	0.32 (12.3%)
O_3+2-Butene	2.79 (18.9%)	0.13 (6.8%)	0.20 (7.5%)
Other	1.22 (8.3%)	0.20 (10.4%)	0.31 (11.7%)
Total	14.77	1.94	2.64

831 The values represent production rates in ppb/hr, with relative percentage contributions provided in parentheses.